

(revised version, submitted to EPSL, 2020-04-24)

3D Multi-source Model of Elastic Volcanic Ground Deformation

Antonio G. Camacho ^a, José Fernández ^{a,*}, Sergey V. Samsonov ^b,
Kristy F. Tiampo ^c, and Mimmo Palano ^d

^a*Institute of Geosciences (CSIC-UCM), C/ Doctor Severo Ochoa, 7, Facultad de Medicina
(Edificio entrepabellones 7 y 8, 4^a planta), Ciudad Universitaria, 28040, Madrid, Spain. (e-
mail: antonio_camacho@mat.ucm.es, jft@mat.ucm.es)*

^b*Canada Centre for Mapping and Earth Observation, Natural Resources Canada, 560
Rochester Street, ON K1A 0E4, Ottawa, Canada. (e-mail: sergey.samsonov@canada.ca)*

^c*CIRES and Geological Sciences. 216 UCB, University of Colorado, Boulder, CO 80309,
USA. (e-mail: kristy.tiampo@colorado.edu)*

^d*Istituto Nazionale di Geofisica e Vulcanologia, Osservatorio Etneo - Sezione di Catania,
Piazza Roma 2, 95125 Catania, Italy (e-mail: mimmo.palano@ingv.it)*

*Corresponding author: jft@mat.ucm.es, +34-913944632 (JF)

Keywords: 3D Model; multi-source; elastic medium; ground deformation.

26 **ABSTRACT:** Developments in Interferometric Synthetic Aperture Radar (InSAR) and GNSS
27 (Global Navigation Satellite System) during the past decades have promoted significant
28 advances in geosciences, providing high-resolution ground deformation data with dense
29 spatio-temporal coverage. This large dataset can be exploited to produce accurate assessments
30 of the primary processes occurring in geologically active areas. We present a new, original
31 methodology to carry out a multi-source inversion of ground deformation data to better
32 understand the subsurface causative processes. A nonlinear approach permits the
33 determination of location, size and three-dimensional configuration, without any a priori
34 assumption as to the number, nature or shape of the potential sources. The proposed method
35 identifies a combination of pressure bodies and different types of dislocation sources (dip-
36 slip, strike-slip and tensile) that represent magmatic sources and other processes such as
37 earthquakes, landslides or groundwater-induced subsidence through the aggregation of
38 elemental cells. This approach has the following features: (1) simultaneous inversion of the
39 deformation components and/or line-of-sight (LOS) data; (2) simultaneous determination of
40 diverse structures such as pressure bodies or dislocation sources, representing local and
41 regional effects; (3) a fully 3D context; and (4) no initial hypothesis about the number,
42 geometry or types of the causative sources is necessary. This methodology is applied to Mt.
43 Etna (Southern Italy). We analyze the ground deformation field derived from a large InSAR
44 dataset acquired during the January 2009 – June 2013 time period. The application of the
45 inversion approach models several interesting buried structures as well as processes related to
46 the volcano magmatic plumbing system, local subsidence within the Valle del Bove and
47 seaward motion of eastern flank of the volcano.

48

49 **1. Introduction.**

50 Recent technical developments in geodesy have resulted in significant advances in
51 volcanology ([Fernández et al., 2017](#); and references therein). For example, Global Navigation
52 Satellite System (*GNSS*) produced sub-centimeter precision in positioning while the
53 development of Advanced Differential Interferometric Synthetic Aperture Radar (*A-DInSAR*)
54 techniques have resulted in the estimation of 1D to 3D deformation field with dense spatio-
55 temporal coverage. Therefore, high resolution, high precision measurements of ground
56 deformation with extensive coverage are available to explore complex models of ground
57 deformation in volcanic areas.

58 In this context, surface displacements are inverted to infer valuable constraints on the
59 active magmatic sources (e.g., [Rymer and Williams-Jones, 2000](#); [Fernández et al., 2001](#);
60 [Dzurisin, 2007](#); [Cannavò et al., 2015](#)). Surface deformation is a direct consequence of the
61 dynamics of volcanic plumbing systems, and reflect the shape of magma intrusions, the
62 volume of intruding/arising magma, and the emplacement mechanisms. Normally, regular
63 geometries (point sources, disks, prolate or oblate spheroids, etc.) are assumed at the initial
64 stages ([Lisowski, 2007](#)) and the resulting inversion is carried out in a linear context.

65 Surface deformation also has been inverted in order to provide insight into the geometry
66 and slip of buried seismic dislocations. The initial geometry of the buried dislocation is
67 generally assumed based on prior information obtained from various sources such as local
68 geology, fault mapping, and earthquake focal mechanisms. Again, the inversion is generally
69 conducted in a linear framework ([Segall, 2010](#); [Pascal et al., 2014](#)).

70 [Camacho et al. \(2011a\)](#) developed an original methodology aimed at the determination of
71 the 3D geometry and the location of the causative bodies by inverting ground deformations
72 and gravity changes due to pressure and/or mass anomalies embedded into an elastic medium.
73 Such a fully nonlinear inversion has led to interesting results in volcanic environments, where

74 ground deformations are related to over-pressured magmatic bodies (Camacho et al., 2011a;
75 Samsonov et al, 2014; Cannavò et al, 2015; Camacho et al., 2018; Camacho and Fernández,
76 2019).

77 Most volcanically active regions are characterized by complicated patterns of ground
78 deformation resulting from multiple natural (e.g., inflation, deflation, dike intrusion, active
79 faulting, flank instability and landslides) and anthropogenic sources (Fernández et al., 2005,
80 2017; Tiampo et al., 2013; Samsonov et al., 2014). For example, Mt. Etna volcano is
81 characterized by short-term inflation/deflation episodes related to the magmatic dynamics of
82 its plumbing system, by a near-continuous seaward motion of its eastern flank (Palano, 2016)
83 and by regional tectonic processes (Palano et al., 2012).

84 An extension of the former successful nonlinear approach, which only estimated elastic
85 deformation due to pressure sources applicable to specific volcanic areas, is required for more
86 general geophysical active regions, where more varied types of deformation sources are
87 present.

88 We present a new inversion process that extends the previous methodology by including
89 dislocation sources as given by Okada (1985), in order to obtain a more general inversion
90 method that estimates non-subjective models of the observed deformation process within an
91 almost entirely automatic framework.

92 Here, we describe this new approach, some simulation cases, and its application to actual
93 ground deformation at Mt. Etna estimated from advanced *A-DInSAR* data. A second test case,
94 the interpretation of the co-seismic deformation for the 2014 earthquake in Napa Valley
95 (California) (Polcari et al., 2017), is presented in the Supplementary Material. The results
96 allow us to evaluate the power of the methodology for 3D multi-source modelling of volcanic
97 deformation data.

98

99

100 **2. Inversion Methodology.**

101 [Camacho et al. \(2011a\)](#) presented an original methodology for simultaneous inversion of
102 displacement determined using terrestrial and/or space techniques and gravity changes,
103 adapted from a previous methodology for gravity inversion ([Camacho et al, 2007 and 2011b](#)).
104 Assuming simple isotropic elastic conditions, the approach determines a general geometrical
105 configuration of pressurized and/or density sources corresponding to prescribed values of
106 anomalous density and pressure. These sources are described as an aggregate of pressure and
107 density point sources, and they fit the entire dataset within some regularity conditions. In this
108 methodology, the representation of single sources as the sum of elementary solutions
109 representing 3D irregular geometries, as is typically done for dislocation sources representing
110 faults ([Segall, 2010](#)). For pressure sources, this is applied by assuming that the model is linear
111 in the pressure perturbation, with an assumed constant value of pressure change, and the
112 media is assumed to be isotropic, allowing for superposition ([Geerstma and Van Opstal, 1973](#);
113 [Brown et al., 2014](#); [Fernández et al., 2018](#)). In a mathematical appropriate way, pressure and
114 mass sources can be combined together ([Rundle, 1982](#); [Fernández and Rundle, 1994](#)). The
115 approach works in a step-by-step growth process that constructs very general geometrical
116 configurations ([Camacho et al., 2007](#); [2011a, b](#)).

117 This approach provided useful results for volcanic areas when deformations come from
118 magmatic sources considered as a combination of pressure and mass variations, if
119 displacement and gravity change data are available; or just pressure sources if only
120 displacement data exist. Nevertheless, for many volcanic regions, observed deformations
121 often are caused by additional phenomena not related to pressurization. These include fault

122 dislocations, sliding and subsidence phenomena that cannot be satisfactorily modelled with
123 the former approach. Therefore, here we propose an improvement of the original inversion
124 methodology which incorporates these new sources, allowing us to obtain a general model of
125 all the observed deformation composed of multiple simultaneous and combined 3D sources.

126 In this new approach, superposition is still allowable for modeling single sources, as in
127 [Camacho et al. \(2011a\)](#). For combination of different sources of the same or different nature,
128 we apply the results of [Pascal et al. \(2014\)](#).

129 The medium is divided into a 3D partition of elemental cells. The aggregation of
130 elemental sources and the superposition of their contribution forms the geometry of the
131 extended causative bodies. One key aspect is to select some simple expressions for cell
132 contribution in order to fit thousands of data points by the superposition of thousands of cells
133 in a short time, thus allowing the methodology to be used for real time monitoring during
134 unrest ([Cannavò et al., 2015](#); [Camacho and Fernández, 2019](#)).

135 ***2.1 Elementary sources. Direct formulae.***

136 We consider a point $P(X,Y,Z)$ located on the surface of a semi-infinite elastic medium
137 where an elemental source is located at (x,y,z) . For the surface deformation due to elemental
138 dislocation sources we use the expressions by [Okada \(1985\)](#), and for the elemental pressure
139 sources we use the expressions by [Geertsma and Van Opstal \(1973\)](#).

140 ***2.1.1. Surface deformation due to shear and tensile elemental dislocations.***

141 Displacements u_x , u_y , u_z at P produced by a buried dislocations point source located at
142 (x,y,z) in an elastic half-space are given by ([Okada, 1985](#)):

143 (a) for strike-slip:

144
$$\begin{pmatrix} u_x \\ u_y \\ u_z \end{pmatrix} = -\frac{U_1 \Delta S}{2 \pi} \left[\frac{3 dx q}{R^5} \begin{pmatrix} dx \\ dy \\ dz \end{pmatrix} + \sin \delta \begin{pmatrix} I_1 \\ I_2 \\ I_4 \end{pmatrix} \right] \quad (1)$$

145 (b) for dip-slip:

146
$$\begin{pmatrix} u_x \\ u_y \\ u_z \end{pmatrix} = -\frac{U_2 \Delta S}{2 \pi} \left[\frac{3 p q}{R^5} \begin{pmatrix} dx \\ dy \\ dz \end{pmatrix} - \sin \delta \cos \delta \begin{pmatrix} I_3 \\ I_1 \\ I_5 \end{pmatrix} \right] \quad (2)$$

147 (c) for tensile:

148
$$\begin{pmatrix} u_x \\ u_y \\ u_z \end{pmatrix} = -\frac{U_3 \Delta S}{2 \pi} \left[\frac{3 q^2}{R^5} \begin{pmatrix} dx \\ dy \\ dz \end{pmatrix} - \sin^2 \delta \begin{pmatrix} I_3 \\ I_1 \\ I_5 \end{pmatrix} \right] \quad (3)$$

149 where:

150 δ : dip angle of the fault plane,

151 α : azimuth angle

152
$$\begin{pmatrix} dx \\ dy \end{pmatrix} = \begin{pmatrix} \sin \alpha & \cos \alpha \\ -\cos \alpha & \sin \alpha \end{pmatrix} \begin{pmatrix} X - x \\ Y - y \end{pmatrix},$$

153
$$dz = Z - z,$$

$$I_1 = \frac{\mu}{\lambda + \mu} dy \left[\frac{1}{R(R + dz)^2} - dx^2 \frac{3R + dz}{R^3(R + dz)^3} \right],$$

$$I_2 = \frac{\mu}{\lambda + \mu} dx \left[\frac{1}{R(R + dz)^2} - dy^2 \frac{3R + dz}{R^3(R + dz)^3} \right],$$

$$I_3 = \frac{\mu}{\lambda + \mu} dx \left[\frac{1}{R^3} \right] - I_2,$$

$$I_4 = \frac{\mu}{\lambda + \mu} \left[-dx dy \frac{2R + dz}{R^3(R + dz)^2} \right],$$

$$I_5 = \frac{\mu}{\lambda + \mu} \left[\frac{1}{R(R + dz)} - dx^2 \frac{2R + dz}{R^3(R + dz)^2} \right],$$

$$\begin{pmatrix} p \\ q \end{pmatrix} = \begin{pmatrix} \sin \delta & \cos \delta \\ -\cos \delta & \sin \delta \end{pmatrix} \begin{pmatrix} dz \\ dy \end{pmatrix},$$

$$R^2 = (X - x)^2 + (Y - y)^2 + (Z - z)^2 = dx^2 + dy^2 + dz^2 = dx^2 + q^2 + p^2.$$

154 **2.1.2. Surface deformation due to a pressure elemental prismatic body.**

155 The simplest method which still provides a good overall estimate of the spatial subsidence
 156 distribution for compacting reservoirs of arbitrary 3D shape and change in reservoir pressure
 157 is based on the lineal elastic theory of nuclei of strain in the half-space (Geertsma and Van
 158 Opstal, 1973). Assuming linearity of the stress-strain relation and isotropy of the material, the
 159 displacements u_x , u_y , u_z at a surface point P due to a buried small prismatic source with
 160 overpressure Δp and sides $\Delta x, \Delta y, \Delta z$, located at (x, y, z) in an elastic half-space can be
 161 determined as:

$$162 \quad \begin{pmatrix} u_x \\ u_y \\ u_z \end{pmatrix} = \Delta p \frac{1-\nu}{\mu} \frac{3}{4\pi} \int_{x-\Delta x/2}^{x+\Delta x/2} \int_{y-\Delta y/2}^{y+\Delta y/2} \int_{z-\Delta z/2}^{z+\Delta z/2} \begin{pmatrix} X - \xi \\ Y - \eta \\ Z - \zeta \end{pmatrix} \frac{d\xi d\eta d\zeta}{((X-\xi)^2 + (Y-\eta)^2 + (Z-\zeta)^2)^{3/2}} \quad (4)$$

163 where ν is the Poisson's ratio and μ is the shear modulus.

164 Assuming that displacements u_x , u_y , u_z at the surface happen to be almost directly
 165 proportional to the thickness Δz of the reservoir, the volume integrations for a parallelepiped
 166 cell of sides Δx , Δy , Δz and overpressure Δp in equations (4) can be simplified to integration in
 167 the horizontal plane only given rise to (Geertsma and Van Opstal, 1973):

$$168 \quad \begin{pmatrix} u_x \\ u_y \\ u_z \end{pmatrix} = \Delta p \frac{1-\nu}{\mu} \frac{3}{4\pi} I \Delta z \quad (5)$$

169 where:

$$170 \quad I = I_i \left(X - x + \frac{\Delta x}{2}, Y - y + \frac{\Delta y}{2}, Z - z \right) - I_i \left(X - x + \frac{\Delta x}{2}, Y - y - \frac{\Delta y}{2}, Z - z \right) -$$

$$171 \quad I_i \left(X - x - \frac{\Delta x}{2}, Y - y + \frac{\Delta y}{2}, Z - z \right) + I_i \left(X - x - \frac{\Delta x}{2}, Y - y - \frac{\Delta y}{2}, Z - z \right),$$

172 and integrals I_i for displacements along i -directions are given by:

173
$$I_z(p, q, r) = \frac{1}{2} \frac{p}{|p|} \frac{q}{|q|} \left\{ \arcsin \frac{p^2 q^2 - r^2 (p^2 + q^2 + r^2)}{(p^2 + r^2)(q^2 + r^2)} + \frac{\pi}{2} \right\},$$

174
$$I_x(p, q, r) = \operatorname{arcsinh} \frac{p}{\sqrt{q^2 + r^2}},$$

175
$$I_y(p, q, r) = \operatorname{arcsinh} \frac{q}{\sqrt{p^2 + r^2}}.$$

176 Equations (1)-(3), (5) provide the surface displacement due to elemental cells for pressure
 177 and dislocations. The total effect of a single anomalous structure described as an aggregation
 178 of m small parallelepiped cells is obtained as an addition (discrete integration) of the partial
 179 effects (Geertsma and Van Opstal, 1973; Okada, 1985).

180 The topography of volcanoes can have an important effect on deformation changes
 181 (Supplementary Material). We take this effect into account by incorporating the varying-
 182 elevation analytical solution approach (Williams and Wadge, 1998) into the equations and
 183 code. This direct formulation is used to carry out the inverse approach and to determine the
 184 pressure and dislocation 3D source structures responsible of the observed deformation.

185 **2.2. Inversion methodology**

186 The perturbing 3D sources are described as an aggregate of elemental sources that fits the
 187 entire dataset within some regularity conditions. The approach works in a step-by-step growth
 188 process (Camacho et al., 2007; 2011b) constructing very general geometrical configurations.

189 The observation equations are:

190
$$\mathbf{dr} = \mathbf{dr}^c + \boldsymbol{\varepsilon} \tag{6}$$

191 where \mathbf{dr} , \mathbf{dr}^c represent the vector of observed and calculated 3D displacements, and $\boldsymbol{\varepsilon}$ the
 192 residual values coming from inaccuracies in the observations and from insufficient model fit.

193 In Camacho et al. (2011a), the surface deformations, \mathbf{dr}^c , due to a buried over pressure
 194 structure are calculated aggregating the effects for several Mogi point sources (Masterlark,

195 2007). In the present paper \mathbf{dr}^c corresponds to the addition of the pressure sources and the
 196 Okada's dislocation sources (strike-slip, dip-slip and tensile). Moreover, we substitute the
 197 simple point source calculus (Masterlark, 2007) by the more accurate calculus by Geertsma
 198 and Van Opstal (1973) for 3D pressure structures.

199 2.2.1. Model description.

200 General geometrical single structures will be described by aggregation of elementary
 201 sources filled with causative perturbations (pressure, and strike-slip, dip-slip and tensile
 202 dislocations). We consider a partition of the medium into a dense 3D grid of m small cells
 203 located in (x_i, y_i, z_i) and with small volumes $\Delta V_i = \Delta x_i \cdot \Delta y_i \cdot \Delta z_i$ and small dislocation
 204 surfaces $\Delta S_i, i=1, \dots, m$. The data spatial resolution conditions the smaller cell size. Each small
 205 cell effect can be modeled by the effect of an elementary source located in its geometric
 206 center. We carry out the partitioning by means of small rectangular prisms on horizontal
 207 layers, looking for a similar average quadratic deformation effect of each cell upon the whole
 208 data set. Then, we calculate the deformation effects, $\mathbf{dr}_j (dX_j, dY_j, dZ_j)$ (see Figure 1), in the n
 209 surface (not necessarily gridded) points, $P_j(X_j, Y_j, Z_j) (j=1, \dots, n)$ by accumulation of the effects
 210 of the filled cells (for $i \in \text{set } \Phi_P$ of pressured, $i \in \text{set } \Phi_S$ of strike dislocation cells, $i \in \text{set } \Phi_D$
 211 for dip-slip and thrust dislocation cells, and $i \in \text{set } \Phi_T$ for tensile dislocation cells):

$$212 \quad \mathbf{dr}^c = \sum_{\Phi_P} \begin{pmatrix} u_x \\ u_y \\ u_z \end{pmatrix} + \sum_{(\Phi_S, \Phi_D, \Phi_T)} \begin{pmatrix} u_x \\ u_y \\ u_z \end{pmatrix} \quad (7)$$

$$213 \quad dr_j^c = \sum_{i \in \Phi_P} \Delta V_i \Delta \rho_i f_p(r_{ij}) + \sum_{i \in \Phi_S} \Delta S_i \Delta \sigma_i f_S(r_{ij}, \alpha_i, \delta_i) + \sum_{i \in \Phi_D} \Delta S_i \Delta \sigma_i f_D(r_{ij}, \alpha_i, \delta_i) +$$

$$214 \quad \sum_{i \in \Phi_T} \Delta S_i \Delta \sigma_i f_T(r_{ij}, \alpha_i, \delta_i) \quad (8)$$

$$215 \quad j=1, \dots, n$$

216 with u_x, u_y, u_z given through equations (1), (2), (3) and (5).

217 Volumes ΔV_i , surfaces ΔS_i and intensity factors $\Delta \rho_i$ (pressure, MPa) and $\Delta \sigma_i$ (dislocation,
 218 cm) appear as linear factors in the observation equations (6)-(8), allowing for simple cell
 219 aggregation, but the other model parameters (orientation angles α and δ , and sets Φ_P , Φ_S , Φ_D ,
 220 and Φ_T of filled cells) are nonlinear, necessitating a non-linear inversion approach.

221 **2.2.2. Misfit conditions.**

222 Assuming a Gaussian uncertainty given by a covariance matrix \mathbf{Q}_D for displacement data,
 223 a minimization condition for observation residuals $\boldsymbol{\varepsilon}$, as $\boldsymbol{\varepsilon}^T \mathbf{Q}_D^{-1} \boldsymbol{\varepsilon} = \min$, leads to the maximum
 224 likelihood solution. For a simplified treatment, \mathbf{Q}_D is considered as a diagonal matrix of
 225 estimated variances corresponding to the displacement data.

226 During inversion of geophysical data, problems of singularity and instability for the
 227 solution can arise due to inadequate data coverage (normally the number of data points is
 228 smaller than the number of unknowns), inaccuracy of the data, and intrinsic ambiguity of the
 229 design problem. In this case, they can occur if we assume that positive and negative
 230 anomalous pressure/dislocations can be contemporaneously present in the model. A process to
 231 avoid instabilities is to consider additional minimization or smoothing conditions for the norm
 232 of the solution model as:

$$233 \quad \mathbf{m}^T \mathbf{Q}_M^{-1} \mathbf{m} = \min, \quad (9)$$

234 where the vector \mathbf{m} is constituted by the values $\Delta \rho_i$ and $\Delta \sigma_i$ ($i=1, \dots, m$) for the filled cells of
 235 the model (sets Φ_P , Φ_S , Φ_D , and Φ_T) and \mathbf{Q}_M is a suitable covariance matrix corresponding to
 236 the physical configuration of cells and data points. This matrix provides a balanced model,
 237 avoiding very shallow solutions. We propose a normalizing diagonal matrix \mathbf{Q}_M with elements
 238 q_i ($i=1, \dots, m$) given for volumes ΔV_i and distances r_{ij} as

239
$$q_i = \frac{\Delta V_i}{n} \sum_{j=1}^n \frac{|z_j - z_i|}{r_{ij}^3}, \quad (10)$$

240 that takes into account the average effect of the i -th cell upon all data points.

241 Condition (9) is a stabilizing term for control on the entire pressure, and dislocations of the
 242 structures (Farquharson and Oldenbourg, 1998; Bertete-Aguirre et al., 2002). Weighting by
 243 matrix \mathbf{Q}_M prevents the occurrence of very large fictitious values of pressure/dislocations,
 244 resulting from a model that is poorly determined model due, e.g., to coupling of some positive
 245 and negative sources, peripheral sources, etc.

246 Finally, a mixed minimization equation

247
$$S(\mathbf{m}) = \boldsymbol{\varepsilon}^T \mathbf{Q}_D^{-1} \boldsymbol{\varepsilon} + \gamma \mathbf{m}^T \mathbf{Q}_M^{-1} \mathbf{m} = \min . \quad (11)$$

248 is adopted for the constraining equation (6) for residuals and for model magnitude. γ is a
 249 factor that provides a balance between fitness and smoothness of the model. Low γ values
 250 produce very good data fit but often result in extended and/or irregular models. Conversely,
 251 high γ values can produce concentrated and smooth models but with a poorer data fit. The
 252 optimal choice is determined by an autocorrelation analysis of the residual values, the value
 253 producing a null (planar) autocorrelation distribution (Moritz, 1980; Camacho et al., 2007).

254 ***2.2.3 Exploration approach for solving the system.***

255 The model system (6)-(8) must be satisfied within the minimization constraint condition
 256 (11). It constitutes a nonlinear optimization problem with respect to the geometrical properties
 257 (orientation angles α and δ for the dislocations, and sets Φ_P , Φ_S , Φ_D , and Φ_T of filled cells).

258 Considering the very large number of degrees of freedom necessary to describe the
 259 pressure and dislocation sources, a general exploratory inversion approach simultaneously
 260 applied to the aggregation of thousands of small cells filled with anomalous values would be

261 ineffective. A necessary reduction of the model space is obtained by limiting the possible
262 orientation angles (dip δ and azimuth α), considering only certain orientations. We limit
263 values of α from 0° to 180° , and of δ from 0° to 90° , with step 10° , resulting in 190 possible
264 orientations for each elemental dislocation. After tests on simulated and real data we have
265 concluded that this offers enough detail for most practical applications. Any arbitrary
266 dislocation direction can be fit by a combination of these basic directions.

267 The model space to be explored is composed by: (1) m possible cells to be filled; (2) four
268 primary source possibilities (pressure change, strike, dip or tensile dislocation) for each cell;
269 (3) positive or negative value for each pressure/dislocation cell; and (4) 190 possible
270 orientations for dislocation elements. As previously pointed, coefficients ΔV_i , ΔS_i , $\Delta \rho_i$ and
271 $\Delta \sigma_i$ appear in linear mode and they are solved by a scaled, linear fit.

272 Despite the reduction in angular options, a general exploration of the extensive model
273 domain that considers all possible combinations of thousands of cells, and angles, signs, and
274 source natures, would be inefficient. An alternative approach is to build the anomalous 3D
275 structures by means of a step-by-step growth process. The key idea is to substitute a unique
276 global exploratory approach by successive explorations. For each step of the growth process,
277 that exploration allows for selection of only one new optimal cell (and additional parameters)
278 (Camacho et al., 2007; 2011b). This approach explores a model domain clearly smaller at
279 every step, composed only of the “empty” cells.

280 Further, we assume that pressure values ($\Delta \rho$) and dislocation amplitude values ($\Delta \sigma$) will be
281 the same over the entire model. These will be expressed as proportional to some basic fixed
282 values $\Delta \rho_o$ and $\Delta \sigma_o$, $\Delta \rho = f \times \Delta \rho_o$ and $\Delta \sigma = f \times \Delta \sigma_o$, $f > 0$ being a scale factor. $\Delta \rho_o$ and $\Delta \sigma_o$ are
283 arbitrary small fixed values with a fixed ratio $\Delta \rho_o / \Delta \sigma_o$ so that the average effect upon the data
284 of an arbitrary cell with dislocation $\Delta \sigma_o$ will be similar to the one of a pressure arbitrary cell
285 with pressure $\Delta \rho_o$.

286 Considering these conditions, we implement the step-by-step growth process. For the k -th
 287 step of the growth process, k cells have been filled with the prescribed anomalous values for
 288 pressure $\Delta\rho_o$ and dislocation amplitude $\Delta\sigma_o$, giving rise to modeled values \mathbf{dr}^c from the model
 289 equations, which now include a scale factor. For the $(k+1)$ -th step, we fill a new cell fitting
 290 the system,

$$291 \quad \mathbf{dr} = f_{k+1} \mathbf{dr}^c + \boldsymbol{\varepsilon} \quad (12)$$

$$292 \quad \boldsymbol{\varepsilon}^T \mathbf{Q}_D^{-1} \boldsymbol{\varepsilon} + \gamma f_{k+1}^2 \mathbf{m}^T \mathbf{Q}_M^{-1} \mathbf{m} = \min, \quad (13)$$

293 where $0 < f_{k+1} < f_k$ is a scale factor that fits the modeled deformation field for the provisional,
 294 not fully developed, model and the observed deformations. We calculate the value
 295 $e^2 = \boldsymbol{\varepsilon}^T \mathbf{Q}_D^{-1} \boldsymbol{\varepsilon} + \gamma f_{k+1}^2 \mathbf{m}^T \mathbf{Q}_M^{-1} \mathbf{m}$ for the empty cells according to a general exploratory approach
 296 with random selection. We choose as optimal cell to be filled for the $(k+1)$ -th step that j -th
 297 cell giving:

$$298 \quad e_j^2 = \min. \quad (14)$$

299 Throughout the process both f and e^2 decrease. Note that considering the scale factor f
 300 modifies the process from a unique general exploration of the extensive model domain, which
 301 would be inefficient, to a much more affordable task: the exploration of aggregation
 302 possibilities for a new cell, in a step-by step growth process. This is the primary feature of the
 303 inversion approach.

304 The process continues until: (1) f reaches a prescribed small value according to a defined
 305 criterion based on previous trials and inspection of the resulting model; or (2) aggregation of a
 306 new cell does not produce smaller values of f and e^2 . Case (2) produce the larger model, with
 307 smaller values for $\Delta\rho$ and $\Delta\sigma$. One potential definition of the stopping criteria could be a
 308 prescribed ratio between successive e^2 values.

309 At the final step, we arrive at a 3D model virtually automatically. That model is the
310 aggregation of some filled elementary cells: (1) pressure elementary sources filled with the
311 prescribed anomalous values; and (2) dislocation elementary sources with the appropriate
312 orientation and magnitude. Together, they fit the observed displacement within some error
313 margin and appropriate set of model bounds.

314 A final test on the validity of the inversion results is done by comparing their geographical
315 distribution and distances between differences sources, as in [Pascal et al. \(2014\)](#).

316 Additional details about the practical implementation of the inversion approach are
317 described in Section B of the Supplementary Material.

318 **3. Synthetic test cases.**

319 To demonstrate the efficiency of this inversion process, we consider a simulated example
320 described in Figure 2, composed of four different deformation sources: a vertical ellipsoid
321 with homogeneous negative pressure (-3 MPa located at 2.5 km depth below the surface and
322 with semi-axes of 2 km and 1.4 km) (Figure 2a); a sub-horizontal strike-slip fault (azimuth
323 65° and dip angle 20° from the horizontal, length 5 km and width 3 km, located at 1.5 km
324 depth) with 12 cm dislocation (Figure 2b); a nearly vertical dip-slip fault (azimuth 30° and tilt
325 angle 20° from the vertical, 4 km vertical side and 7 km horizontal side, mean depth 2.5 km
326 below the surface) with 9 cm dislocation (Figure 2c); and a tensile fault (azimuth 20° , tilt
327 angle 5° , dimensions 2 km and 4 km, mean depth 2 km) with 10 cm of opening (Figure 2d).
328 Above these buried anomalous structures, a planar distribution grid of 800 data points is
329 delineated, with a grid size of 400 m and total diameter of 12 km (Figure 3). The anomalous
330 pressure body, which is sensitive to the diameter of the survey area, occupies a central
331 position below the survey area. The fault structures are located in the borders of the survey
332 area. In this case, we employ a magnitude of 6 MPa (for pressure) and 9 cm (for all
333 dislocation kinds). Figure 3 shows the (a) Up , (b) EW and (c) NS components of the simulated

334 displacement vectors (u_x, u_y, u_z) at the 800 surface points (X_i, Y_i, Z_i) . The average amplitudes
335 of these 800 data values are 2.1 cm, 1.2 cm, and 1.4 cm respectively.

336 For the simulated data (Figure 3), we apply the inversion approach without any a priori
337 assumptions about the 3D structure of the sources. First, we determine a complete 3D
338 partition of the subsurface volume into several thousands of cells with mean side 170 m
339 (Figure 1). The primary decision required concerns the γ parameter. It is selected, after several
340 trials, as that larger value producing a (nearly) null autocorrelation distribution of the final
341 residues for the three components. A secondary assessment is made for the growth stopping
342 criteria. Here we employ a standard threshold value for the ratio e_k^2/e_{k-1}^2 between successive
343 values of the misfit parameter, given as a default value in our software. Once these are
344 selected, the 3D model for the deformation sources is obtained automatically. This resulting
345 model is composed of a large aggregation (thousands) of elementary (pressure and
346 dislocations) cells. Figure 3 (right) shows the fit between the simulated (orange) and modelled
347 (blue) data. That fit is quite good, about 0.01 cm for all three components.

348 Figure 4 shows a flat view from the top of the obtained 3D model defined by aggregation
349 of elemental deformation sources. They reproduce the simulated data (Figure 3) very well and
350 fit the original simulated, pressurized ellipsoid and faults, represented by dashes lines in
351 Figure 4, reasonably well, given that the inversion fit is unconstrained, and involves several
352 simultaneous possibilities for the active structures without specific a priori hypothesis about
353 the number, nature or shape of sources.

354 Considering these results, we outline some observations on the operation of this
355 methodology:

356 (1) The SE dipping fault structure appears well-constrained, almost entirely composed of
357 small dipping elements (yellow in Figures 4 and 5), whose aggregation describes an
358 extended body with geometry and location similar to the original body. As expected,

359 considering the regularity conditions, the top of the structure is quite precise, but the
360 bottom appears rounded and more diffuse.

361 (2) The pressure ellipsoidal structure also is well-characterized, composed largely of an
362 aggregation of pressure cells (dark blue in Figures 4 and 5) and with geometry and
363 location similar to the original body.

364 (3) The NW sub-horizontal strike structure also is identified and modelled in the inversion
365 approach, composed of an aggregation mostly strike elements (green in Figures 4 and
366 5). Nevertheless, the sub-horizontal character of the original structure provided some
367 difficulties, and we observe a large number of dipping cells whose effect, for sub-
368 horizontal structures and limited values of orientation angles, could be close to those
369 of strike cells. The geometry also is less precise than for the SE nearly vertical
370 structure.

371 (4) The tensile structure is the least faithful model here (Figures 4 and 5), composed
372 primarily by tensile cells but with some distortions.

373 A well-understood drawback to and unconstrained inversion is that there is a known
374 ambiguity regarding the true values of the magnitude of the sources (MPa for pressure and cm
375 for displacement). The same deformation values can be reproduced with a high magnitude or
376 intensity at deeper depth as with smaller, more shallow structures. Here this issue is related to
377 the selection of the stopping point for the growth of the model.

378 In the Supplementary Material, Section C, we show additional synthetic cases. First, we
379 show the inversion results for the former source bodies, but as isolated structures, and an
380 isolated spherical source. These isolated studies offer better results than the former combined
381 modelling. Second, we present different simulation studies for combinations of spherical
382 pressurized bodies. Third, we repeat the previous synthetic case combining different
383 structures, but adding a high level of synthetic Gaussian noise to the data (about a 33%).

384 Results show the efficiency in noise filtering, but they also show some deterioration of the
385 model due the noise effects. All this material provides an evaluation of the method's efficacy.

386 An additional consideration is that of the relative confidence corresponding to the fitted
387 model. First, a global confidence of the model comes, as previously pointed out, from the
388 study of the autocorrelation of the residuals and the choice of the value of the smoothing
389 parameter γ . Another interesting approach to the model confidence comes from a study of the
390 sensitivity of the data pixels to the different areas of the 3D model. Indeed, the model
391 characteristics (nature of the source, magnitude, orientation angles, sign) are identified with
392 varying clarity depending on the location of the cells within the subsurface volume and the
393 orientation of the dislocation sources. Cells located in very deep or peripheral areas with
394 respect to the pixels provide a smaller sensitivity and relative confidence (Supplementary
395 Material, Section E).

396 ***4. Mt. Etna application case.***

397 Mt. Etna (Figure 6) constitutes an excellent test case for applying the inversion
398 methodology detailed above. The volcano was characterized, over the past decade, by
399 persistent volcanic activity as well as a continuous seaward motion of its eastern flank
400 (Palano, 2016). In addition, the large number of SAR images over the region provides a high
401 quality dataset of ground deformation at the scale of the entire volcano. We perform an
402 application of the inversion methodology without a priori assumptions on the numbers, type
403 and 3D geometry of the causative sources.

404 ***4.1. Deformation data.***

405 To study ground deformation at Mt. Etna we collected 38 ascending and 59 descending
406 RADARSAT-2 Standard-3 (S3) images spanning the January 2009 - June 2013 period (see

407 Figure 7, and Table S1, Supplementary Material, Section D). Each SAR dataset was
408 processed independently with the GAMMA software (Wegmuller and Werner, 1997). A
409 single master for each set was selected and remaining images were re-sampled into the master
410 geometry. The spatially averaged interferograms were computed and the topographic phase
411 was removed using the 30 m resolution Advanced Spaceborne Thermal Emission and
412 Reflection Radiometer (ASTER) Digital Elevation Model. Differential interferograms were
413 filtered using adaptive filtering with a filtering function based on local fringe spectrum
414 (Goldstein and Werner, 1998) and unwrapped using the minimum cost flow algorithm
415 (Costantini, 1998). The residual orbital ramp was corrected by applying a baseline refinement
416 algorithm implemented in GAMMA software. For this, the area experiencing large ground
417 deformation was masked out and baseline parameters were re-estimated from the
418 measurements of interferometric phase and topographic height. Minor interpolation of each
419 interferogram was performed in order to improve the spatial coverage reduced by
420 decorrelation. Then, 494 ascending and 298 descending interferograms were geocoded and
421 resampled to a common lat/long grid with the uniform spatial sampling (Table 1). The
422 advanced Multidimensional Small BAseline Subset (MSBAS) method (Samsonov and
423 d'Oreye, 2012; Samsonov et al., 2014) was employed to produce horizontal and vertical time
424 series of ground deformation.

425 Several inflation/deflation episodes occurred during the 2009-2013 period. However, the
426 GNSS time series show a clear long-term trend, similar to the InSAR average deformation
427 rates. Therefore, as a first order approximation, use of the average deformation rates to
428 describe the long-term trend is justified. Working directly with ascending and descending
429 *LOS* displacements would avoid some uncertainties but it would make interpretation of results
430 significantly more tedious. Two-dimensional deformation rates produced by MSBAS can be
431 easily understood by any user, independently of their knowledge on InSAR.

432 From the total dataset (approximately 451000 pixels) for both Up and EW components, we
433 extract a reduced subset as input for the inversion approach. We use pixels which verify three
434 conditions: located within 20 km distance from the Mt. Etna summit, with a distance between
435 consecutive pixels of 800 m, and with a coherence value higher than 0,6. The result of this
436 selection is a dataset of 1613 pixels (Figure 7). At this reduced size the inversion method runs
437 faster and the main features of the resulting model will be nearly the same that for the total
438 dataset (see Supplementary Material).

439 **4.2 Inverse modelling.**

440 We apply the inversion approach as in the simulated examples, without any assumptions
441 about the nature of the active elements, although we only use two displacement components
442 (Up and EW) obtained from the InSAR data. First, we consider a 3D partition of the
443 subsurface volume into several thousands of small cells, with an average side of 500 m. As in
444 the synthetic test case, the only one decisions to take before to carry out the inversion involve
445 the selection of the value for the smoothing γ parameter (we apply a trial study about
446 correlation of residuals) and a value (our usual default value) for determining the growth end.

447 Figure 7 shows the data fit for both components (Up and EW) corresponding to the
448 selected ground deformation data for the considered period (orange dots, Figure 7). The
449 remaining residuals do not contain significant spatial autocorrelation, and their standard
450 deviations are approximately 0.1 cm/yr. It is interesting to observe that the proposed inversion
451 approach allows for the identification of data noise and outlier values, while modelling the
452 deformation signal (blue dots, Figure 7). The inversion approach helps to separate
453 perturbations in the deformation data, such as inexact orientation or regional effects. In fact,
454 in such cases, the model will introduce fictitious sources, located in very shallow or very
455 peripheral locations, limiting distortion effects on the real sources.

456 The resulting 3D model is composed of approximately 12,000 cells filled with one of the
457 deformation elemental patterns: negative or positive pressure and/or dislocation (with values
458 of about 0.5 MPa and 2 cm) for the available directions, plus several thousands of empty cells
459 (see Figures 8-10).

460 **4.3 Discussion.**

461 The final cell aggregation appears as a rather complex model (Figure 8). However, by
462 isolating subareas and dynamic components of this combined model, the resulting structures
463 identify several interesting features and support several conclusions about the active sources
464 below Mt. Etna volcano.

465 One important caution is that the input data correspond only to the *Up* and *EW*
466 displacement components, neglecting the *NS* component. But the aim of this paper is not to
467 carry out a complete analysis of Mt. Etna sources. We use this case study in order to show an
468 example of the efficiency and robustness of the method. A detailed discussion about the
469 inversion results would be the objective of another paper. Below we briefly discuss the main
470 sources of deformation inferred from our InSAR data modelling.

471 **4.3.1 Plumbing system.**

472 In Figure 9, we show some isolated source structures (pressure and tensile cells) that may
473 be related to the plumbing system of Mt. Etna. These appears to be composed of two echelon
474 pressurized reservoirs located at depths of approximately 3000 and 11000 m below sea level,
475 bsl, and a shallower SSW elongated dike structure at a mean depth of 1500 km bsl (Figures 8-
476 10). These plumbing structures are located below the western slope of the volcano edifice.
477 The deeper reservoirs are located progressively more SSW, suggesting an ancient location of
478 the eruptive system. Their overall shape and position correspond to the crustal volume where
479 a number of inflating/deflating sources, feeding the volcanic activity during 2009-2013, have

480 been inferred by GNSS-based models (e.g. Patanè et al., 2013; Spampinato et al., 2015;
481 Cannata et al., 2015).

482 Curiously, the shallower structure connected with the plumbing system in this model is a
483 tensile elongated structure (purple color in Figures 8-10), located at approximately 1500 m
484 bsl, that seems to extend almost into the volcano summit. Considering that it is located in an
485 area that is sensitive to this modelling method (Supplementary Material, Section E), we infer
486 that it corresponds to dike structures, separate from the deeper reservoir structures that
487 appears as pressurized cells. Such a structure aligns with the so called “West Rift”, a zone of
488 weakness on the western flank where numerous monogenetic pyroclastic cones are aligned
489 along 240-260°N (e.g. Mazzarini and Armienti, 2001).

490 ***4.3.2 Pernicana fault and sliding system.***

491 Our model also suggests a complex pattern of deformation on the eastern flank of the
492 volcano. In the aggregation model shown in Figures 8 and 10, the main source components
493 are cells for strike- and dip slip dislocations. There is a shallower strike system close to the
494 Pernicana fault (Figure 6), which shows a tilted geometry (see Figure 10e) and a deeper sub-
495 horizontal central striking system at a depth about 4 -5 km (Figure 10c). There is also a
496 dipping system in three parts (Figure 10): (a) the shallow header of the downward sliding,
497 both close to the summit (Figure 10a), and inside Valle del Bove (Figure 9b), (b) an intense
498 downward dipping region at 4 km depth (Figure 10c), and (c) a third dipping zone (5 km
499 depth) that corresponds to the thrusting final section of the sliding system.

500 The strike cells largely correspond to sub-horizontal sliding, and the dip cells determine
501 the dipping pattern (normal in the header and Valle del Bove, and thrusting in the last half).
502 We observe that sub-horizontal dislocations dip and strike sources are combined, similar to
503 the synthetic case.

504 This geometry is rather different from that proposed in the literature, resulting from
505 geophysical-geochemical and magnetotelluric data (e.g. [Siniscalchi et al., 2012](#)) and geodetic
506 inversion models (e.g., [Palano, 2016 and references therein](#)). The seaward motion of eastern
507 flank of the volcano occurs along a shallow sliding surface bounded by the North Rift -
508 Pernicana fault system and the South Rift - Mascalucia - Tremestieri - San Gregorio -
509 Acitrezza fault system, northward and southward, respectively (e.g. [Palano, 2016](#)). Since no a
510 priori constraints have been adopted during the inversion, the south-dipping planar surface
511 resulting from the inversion probably represents an “average source” of the sub-horizontal
512 sliding surface and the $\sim 60^\circ$ S-dipping Pernicana fault system. However, where the modelled
513 planar dislocation intersects the volcano surface corresponds to the Pernicana fault system,
514 capturing the boundary between the undeformed sector (northward of the fault) and the
515 unstable region of the eastern flank of the volcano.

516 The localized subsidence structure below Valle del Bove, represented by dip cells and a
517 depressurized body, may be related to: (i) the cooling and compaction of the lava flows that in
518 the last decade accumulated on the western side of Valle del Bove (e.g. [De Beni et al., 2015](#)),
519 and/or (ii) a process of relaxation of the substrate in response to loading produced by
520 deposited lavas (e.g. [Briole et al., 1997](#)).

521 **5. Conclusions.**

522 We have presented a new inversion methodology for modeling geodetic displacement
523 data in active volcanic areas which permits simultaneous inversion of the several components
524 of surface deformations and allows for a global fit of the data. Non-planar and non-gridded
525 data can be employed in this approach.

526 The method allows for objective modelling of diverse causative structures as pressure
527 bodies, and general dislocations (strike-slip, dip-slip and tensile). Well-known analytical

528 expressions from [Okada \(1985\)](#), for elemental dislocation sources, and [Geertsma and Van](#)
529 [Opstal \(1973\)](#), for pressured small prisms, are used for direct calculation. They assume a
530 semi-infinite elastic medium, characterized by some values of the elastic parameters. The
531 assumptions of linear elasticity and isotropy allows for the final modeling by superposition of
532 effects for elemental components (prisms and dislocations) form the obtained aggregated
533 geometry.

534 The approach works in a fully 3D context, although it employs, for faster operation,
535 elementary dislocation sources limited to a discrete set of orientations. A free 3D geometry of
536 the causative structures is described by aggregation of small elemental cells. There are not
537 additional a priori requirements on the geometry and types of the causative sources. The
538 method is able to automatically determine the number, nature and 3D geometry of the
539 causative source structures, and supports different type of deformation data, such as
540 *GNSS/GPS*, *InSAR* (horizontal and vertical components, or ascending and/or descending *LOS*
541 data), leveling data, and others. The inversion process constitutes an interesting tool for
542 integrating simultaneously terrestrial and spatial data, providing mapped models which
543 incorporate all the available data.

544 This new methodology allows for a nearly automatic approach that takes advantage of
545 the large and precise datasets coming from ground-based deformation and advanced *DInSAR*
546 techniques and carries out an exhaustive inversion of ground deformation data to better
547 understand the subsurface causative structures and elastic processes, without preconceived
548 hypotheses. It can be applied on large regional scales to model tectonic plate movements and
549 subduction, volcanic activity and, on more local scales, to model deformation from landslides,
550 volcanic eruptions, and anthropogenic subsidence due to mining and extraction of oil, gas, or
551 groundwater. Additionally, this new inversion methodology can be used to invert coseismic
552 geodetic deformation data, as detailed in Section F, Supplementary Material.

553 In particular, for the InSAR data of Mt. Etna 2009-2013, the application of this
554 methodology resulted in a model for several subsurface sources corresponding to the
555 plumbing system, the subsidence within Valle del Bove and the seaward motion of the eastern
556 flank of the volcano.

557 Several precautions should be noted. First, as for other geophysical inversions, the
558 problem has an intrinsic ambiguity. It is solved by use of regularity conditions. Solutions must
559 be interpreted carefully as informative models constrained by limitations in data and
560 smoothing constraints, particularly when applied, as here, within a range of potential
561 causative sources. Second, confidence in the solutions is not uniform. Peripheral or very deep
562 elements will be relatively less valuable (Supplementary Material, Section E). Third, in some
563 cases this approach allows for the separation of perturbing effects (noise, outliers, etc.) in the
564 deformation data.

565 Finally, there are some potential limitations on the validity of the results depending on
566 the combination and sizes of the detected sources. The resulting combination of 3D sources,
567 nature, geometries and relative distances should be examined for inconsistent results, as
568 described in [Pascal et al. \(2014\)](#).

569 *Acknowledgements*

570 This research has been primarily supported by the Spanish Ministerio de Ciencia,
571 Innovación and Universidades research project DEEP-MAPS (RTI2018-093874-B-I00) and
572 partially by the Spanish Ministry of Economy and Competitiveness research project
573 AQUARISK (ESP2013-47780-557-C2-1-R) and Thematic Network EPOS Spain (CGL2016-
574 81965-REDT), and the EU VII Framework Program, ESFRI, EPOS IP (676564-EPOS IP).
575 Research by KFT is funded by CIRES, University of Colorado Boulder. We thank M. Polcari

576 and J. Escayo for providing the 3D coseismic deformation data for the 2014 Napa Valley
577 earthquake. This is a contribution to the Moncloa Campus of International Excellence.

578

579

580 **References**

581 Bertete-Aguirre, H., Cherkaev, E. and Oristaglio, M. (2002), Non-smooth gravity problem
582 with total variation penalization functional, *Geophys. J. Int.*, 149, 499-507.

583 Briole, P., Massonnet, D., Delacourt, C. (1987), Post-eruptive deformation associated with the
584 1986–87 and 1989 lava flows of Etna detected by radar interferometry. *Geophysical*
585 *research Letters*, 24, 37-40, doi:10.1029/96GL03705.

586 Brown, N. J., Woods, A. W., Neufeld, J. A. & Richardson, C. (2014), Constraining Surface
587 Deformation Predictions Resulting from Coal Seam Gas Extraction,
588 <https://doi.org/10.11636/Record.2014.044>.

589 Camacho, A.G., Nunes, J.C., Ortiz, E., França, Z., and Vieira, R. (2007), Gravimetric
590 determination of an intrusive complex under the Island of Faial (Azores): some
591 methodological improvements, *Geophys. J. Int.*, 171, 478–494.

592 Camacho, A.G., González, P.J., Fernández, J. and Berrino, G. (2011a), Simultaneous
593 inversion of surface deformation and gravity changes by means of extended bodies with
594 a free geometry: Application to deforming calderas, *J. Geophys. Res.*, 116, B10401,
595 doi:10.1029/2010JB008165.

596 Camacho, A.G., Gottsmann, J. and Fernández, J. (2011b), The 3-D gravity inversion package
597 GROWTH2.0 and its application to Tenerife Island, Spain, *Computer & Geosciences*,
598 37,621–633

599 Camacho, A. G., Fernández, J. & Cannavò, F. (2018), PAF: A software tool to estimate free-
600 geometry extended bodies of anomalous pressure from surface deformation data.
601 *Comput. Geosci.* 111, 235–243.

602 Camacho, A.G., Fernández, J. (2019), Modeling 3D free-geometry volumetric sources
603 associated to geological and anthropogenic hazards from space and terrestrial geodetic
604 data. *Remote Sens.*, 11(17), 2042; <https://doi.org/10.3390/rs11172042>.

605 Cannata, A., G. Spedalieri, B. Behncke, F. Cannavò, G. Di Grazia, S. Gambino, S. Gresta, S.
606 Gurrieri, M. Liuzzo, and M. Palano (2015), Pressurization and depressurization phases
607 inside the plumbing system of Mount Etna volcano: Evidence from a multiparametric
608 approach, *J. Geophys. Res. Solid Earth*, 120, doi:10.1002/2015JB012227.

609 Cannavò F., Camacho, A.G., González, P.J., Mattia, M., Puglisi, G. & Fernández, J. (2015),
610 Real Time Tracking of Magmatic Intrusions by means of Ground Deformation
611 Modeling during Volcanic Crises. *Scientific Reports*, 5:10970, doi: 10.1038/srep10970.

612 Costantini, M (1998), A novel phase unwrapping method based on network programming.
613 *IEEE Transactions on Geoscience and Remote Sensing*, 36(3):813-821.

614 De Beni, E., B. Behncke, S. Branca, I. Nicolosi, R. Carluccio, F. D’Ajello Caracciolo, and M.
615 Chiappini (2015), The continuing story of Etna’s New Southeast Crater (2012–2014):
616 Evolution and volume calculations based on field surveys and aerophotogrammetry, *J.*
617 *Volcanol. Geotherm. Res.*, 303, 175-186, doi:10.1016/j.jvolgeores.2015.07.021.

618 Dzurisin D. (2007), A comprehensive approach to monitoring volcano deformation as a
619 window on the eruption cycle, *Rev. Geophys.*, 41(1), 1001, doi:10.1029/2001RG000107.

620 Farquharson, C.G., and Oldenbourg, D.W. (1998), Non-linear inversion using general
621 measures of data misfit and model structure, *Geophys. J. Int.*, 134, 213-227.

622 Fernández, J., and Rundle, J.B. (1994), Gravity changes and deformation due to a magmatic
623 intrusion in a two-layered crustal model. *Journal of Geophysical Research*, 99, 2737-
624 2746, doi: 10.1029/93JB02449.

625 Fernández, J., Tiampo, K. F., Jentzsch, G., Charco, M., Rundle, J. B. (2001), Inflation or
626 deflation? New results for Mayon volcano applying elastic-gravitational modeling.
627 *Geophysical Research Letters*, 28, 2349-2352. DOI: 10.1029/2000GL012656.

628 Fernández, J., Romero, R., Carrasco, D., Tiampo, K., Rodriguez-Velasco, G., Aparicio, A.,
629 Araña, V., González-Matesanz, F. (2005), Detection of displacements in Tenerife
630 Island, Canaries, using radar interferometry, *Geophysical Journal International* 160:
631 33-45.

632 Fernández, J., Pepe, A., Poland, M.P., Sigmundsson, F. (2017), Volcano Geodesy: Recent
633 developments and future challenges. *Journal of Volcanology and Geothermal Research*,
634 344, 1-12, doi: 10.1016/j.jvolgeores.2017.08.006.

635 Fernández, J., J. F. Prieto, J. Escayo, A. G. Camacho, F. Luzón, K. F. Tiampo, M. Palano, T.
636 Abajo, E. Pérez, J. Velasco, T. Herrero, G. Bru, I. Molina, J. López, G. Rodríguez-
637 Velasco, I. Gómez, J. J. Mallorquí (2018), Modeling the two- and three-dimensional
638 displacement field in Lorca, Spain, subsidence and the global implications. *Scientific*
639 *Reports*, 8:14782, <https://www.nature.com/articles/s41598-018-33128-0>.

640 Geertsma, J. & Van Opstal, G. (1973), A numerical technique for predicting subsidence above
641 compacting reservoirs based on the nucleus of strain concept. *Verh. Kon. Ned. Geol.*
642 *Mijnbouw* 28, 63–78.

643 Goldstein, R. and Werner, C. (1998), Radar interferogram filtering for geophysical
644 applications. *Geophysical Research Letters*, 25(21):4035-4038.

645 Lisowski, M. (2007), Analytical volcano deformation source models, in *Volcano*
646 *Deformation*, chap. 8, pp. 279-304, Springer Praxis, Chichester, U.K.

647 Masterlark, T. (2007), Magma intrusion and deformation predictions: Sensitivities to the
648 Mogi assumptions, *J. Geophys. Res.*, 112 (B06419), doi:10.1029/2006JB004860.

649 Mazzarini, F., and P. Armienti (2001), Flank cones at Mount Etna volcano: Do they have a
650 power law distribution?, *J. Volcanol. Geotherm. Res.*, 62, 420-430.

651 Moritz, H. (1980). In: Herbert, W.V. (Ed.), *Advanced Physical Geodesy*. Karlsruhe,
652 Germany, p. 500.

653 Okada, Y. (1985), Surface deformation due to shear and tensile faults in a halfspace, *Bull.*
654 *Seismol. Soc. Amer.*, 75, 1135–1154.

655 Palano M., Ferranti L., Monaco C., Mattia M., Aloisi M., Bruno V., Cannavò F., Siligato G.
656 (2012), GPS velocity and strain fields in Sicily and southern Calabria, Italy: Updated
657 geodetic constraints on tectonic block interaction in the central Mediterranean. *Journal*
658 *of Geophysical Research, Solid Earth*, 117, B07401, doi:10.1029/2012jb009254.

659 Palano M. (2016), Episodic slow slip events and seaward flank motion at Mt. Etna volcano
660 (Italy). *Journal of Volcanology and Geothermal Research*, 324, 8-14,
661 doi:10.1016/j.jvolgeores.2016.05.010.

662 Pascal, K.; Neuberg, J.; Rivalta, E. (2014), On precisely modelling surface deformation due to
663 interacting magma chambers and dykes. *Geophys. J. Int.*, 196, 253–278, doi:
664 10.1093/gji/ggt343.

665 Patanè, D., Aiuppa, A. Aloisi, M., Behncke, B., Cannata, A., Coltelli, M., Di Grazia, G.,
666 Gambino, S., Gurrieri, S., Mattia, M., Salerno, G. (2013), Insights into magma and fluid
667 transfer at Mount Etna by a multiparametric approach: A model of the events leading to
668 the 2011 eruptive cycle, *J. Geophys. Res. Solid Earth*, 118, 3519–3539,
669 doi:10.1002/jgrb.50248.

670 Polcari, M., Fernández, J., Albano, M., Bignani, C., Palana, M., Stramondo, S. (2017), An
671 improved data integration algorithm to constrain the 3D displacement field induced by
672 fast deformation phenomena tested on the Napa Valley earthquake. *Computers and*
673 *Geosciences* 109, 206–215.

674 Rundle, J.B. (1982), Deformation, gravity and potential changes due to volcanic loading of
675 the crust. *Journal of Geophysical Research* 87 (B13), 10729–10744 (Correction: *Journal*
676 *of Geophysical Research* 88(B12), 1983, 10647–10652).

677 Rymer, H and Williams-Jones, G. (2000), Volcanic eruption prediction: Magma chamber
678 physics from gravity and deformation measurements. *Geophys. Res. Lett.*, 27, 16, 2389-
679 2392.

680 Samsonov, S., and N. d'Oreye (2012), Multidimensional time series analysis of ground
681 deformation from multiple InSAR data sets applied to Virunga volcanic province,
682 *Geophys. J. Int.*, 191, 1095–1108, doi:10.1111/j.1365-246X.2012.05669.x.

683 Samsonov, S. V., K. F. Tiampo, A. G. Camacho, J. Fernández, and P. J. González (2014),
684 Spatiotemporal analysis and interpretation of 1993–2013 ground deformation at Campi
685 Flegrei, Italy, observed by advanced DInSAR, *Geophys. Res. Lett.*, 41,
686 doi:10.1002/2014GL060595.

687 Segall, P. (2010), *Earthquake and Volcano Deformation*. Princeton University Press,
688 Princeton and Oxford (432 pp., ISBN 978-0-691-13302-7).

689 Siniscalchi, A., S. Tripaldi, M. Neri, M. Balasco, G. Romano, J. Ruch, and D. Schiavone
690 (2012), Flank instability structure of Mt. Etna inferred by a magnetotelluric survey, *J.*
691 *Geophys. Res.*, 117, B03216, doi:10.1029/2011JB008657.

692 Tiampo, K.F., González P.J., Samsonov S. (2013), Results for aseismic creep on the Hayward
693 fault using polarization persistent scatterer InSAR. *Earth Planet. Sc. Lett.*, 367, 157–
694 165.

695 Wegmuller, U. & Werner, C. (1997), GAMMA SAR processor and interferometry software.
696 In *The 3rd ERS symposium on space at the service of our environment*, Florence, Italy.

697 Williams, C. & Wadge, G. (1998), The effects of topography on magma chamber deformation
698 models: Application to Mt. Etna and Radar Interferometry, *Geophys. Res. Lett.*, 25,
699 1549–1552, doi: 0094-8534/98/98GL-011365.

700

701

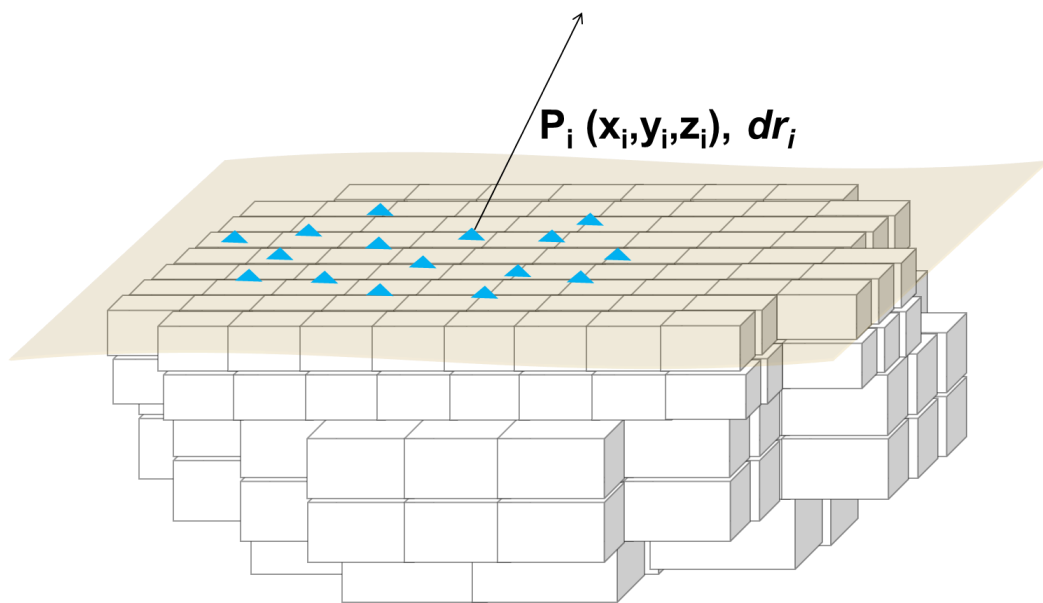
702 **Figures**

703

704

705

706



707

708 **Figure 1.** Partition of the subsurface volume below the survey into a 3D grid of thousands of
709 small right prisms. Blue triangles correspond to data points (terrestrial stations or pixels) P_i
710 with coordinates (x_i, y_i, z_i) and observed deformation vector dr_i .

711

712

713

714

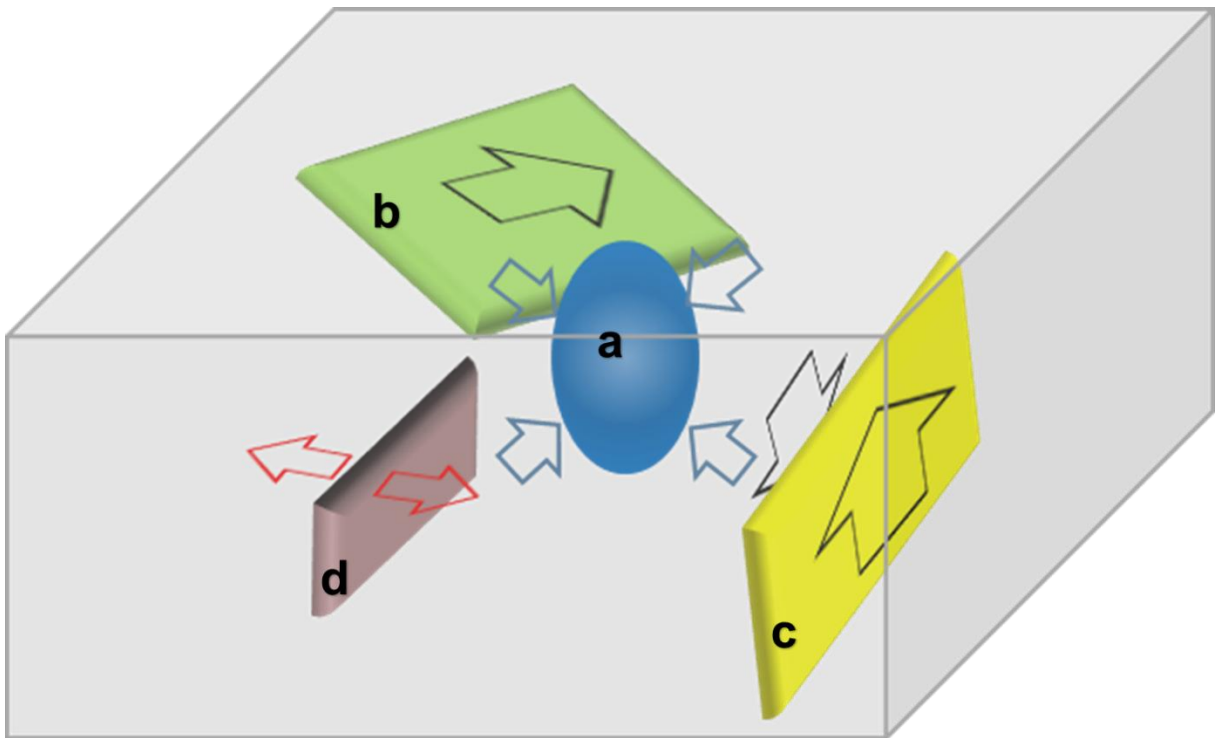
715

716

717

718

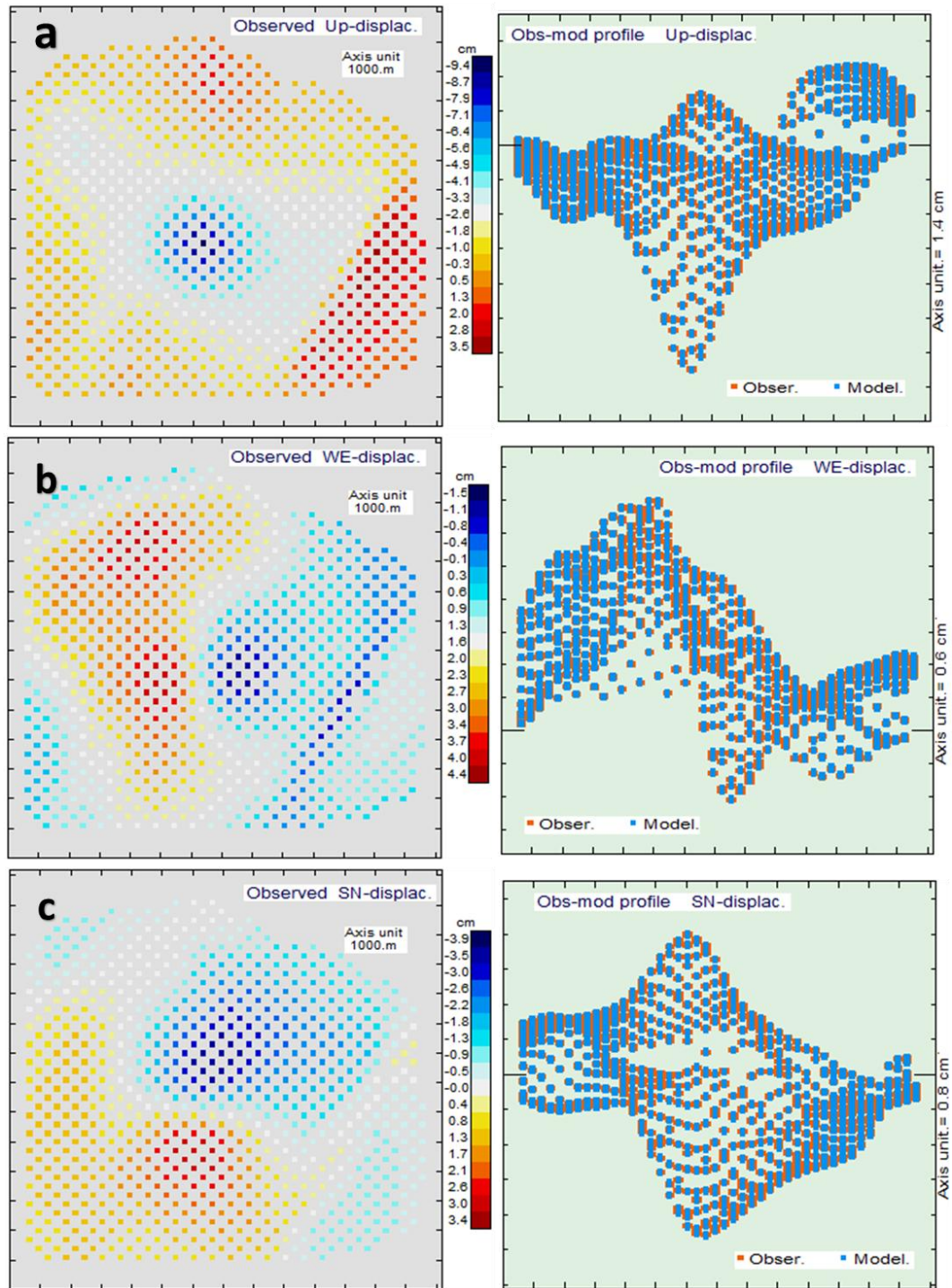
719



720

721 **Figure 2.** Synthetic source structure composed by: (a) a vertical ellipsoid with a
722 decreasing pressure (blue), (b) a sub-horizontal strike slip fault (green), (c) a nearly vertical
723 dip slip fault (yellow), and (d) a nearly vertical tensile fault (brown). See text for details on
724 the sources characteristics.

725

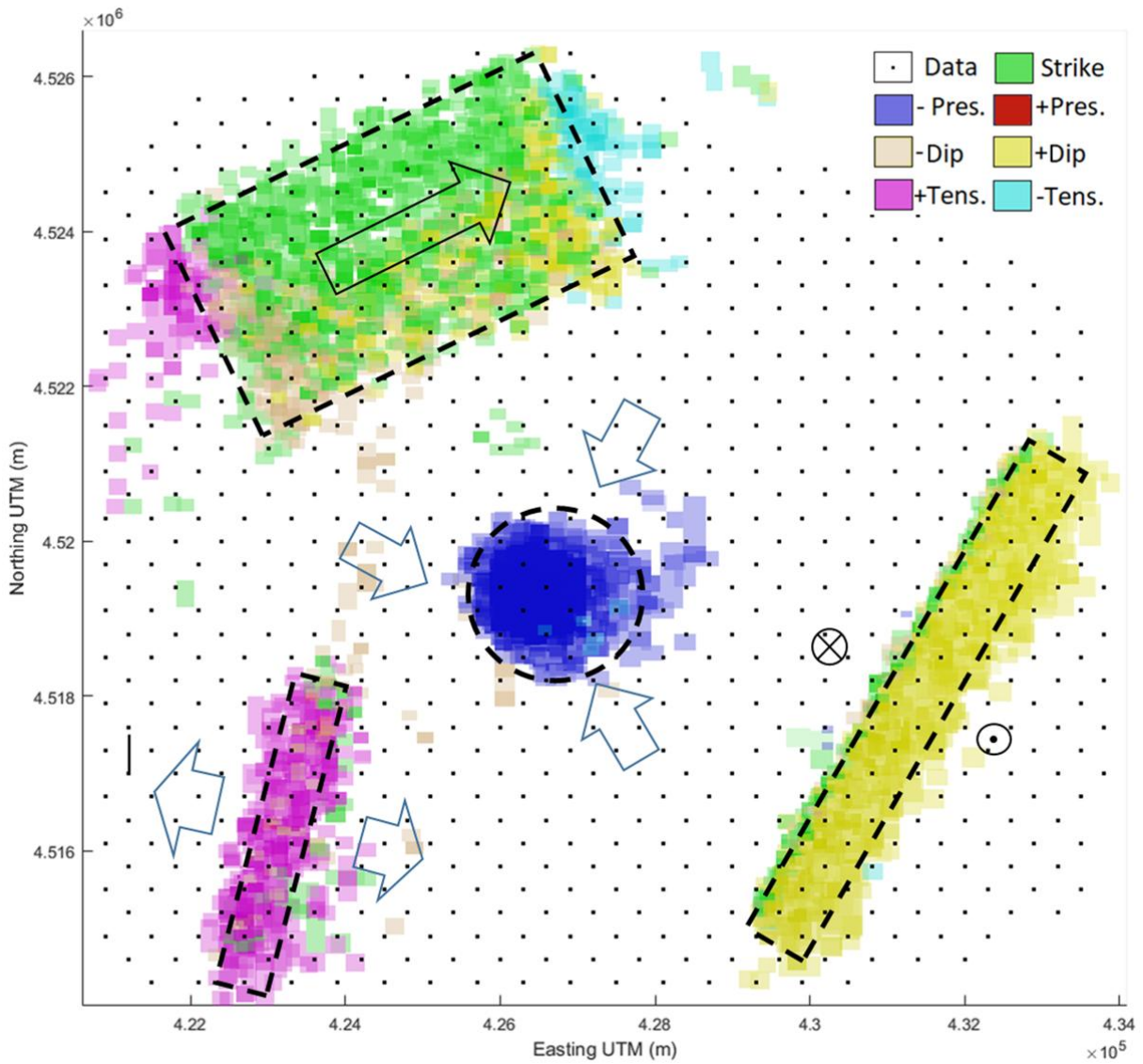


726

727 **Figure 3.** Left panels show the simulated deformation values corresponding to the active
 728 structures shown in figure 2 for the 800 data points used for inversion. (a) Up component. (b)
 729 EW component. (c) NS component. Right panels show the data fit corresponding to the
 730 inverse model for each component. Observed data are plotted in orange, modelled in blue.

731

732



733

734 **Figure 4.** Horizontal view from the top of the resulting source structures, described as
735 aggregation of different elemental source cells, and obtained by application of the inverse
736 approach. Dots indicate data sites, and discontinue lines the location of the synthetic bodies.
737 Arrows show displacement patterns for sources.

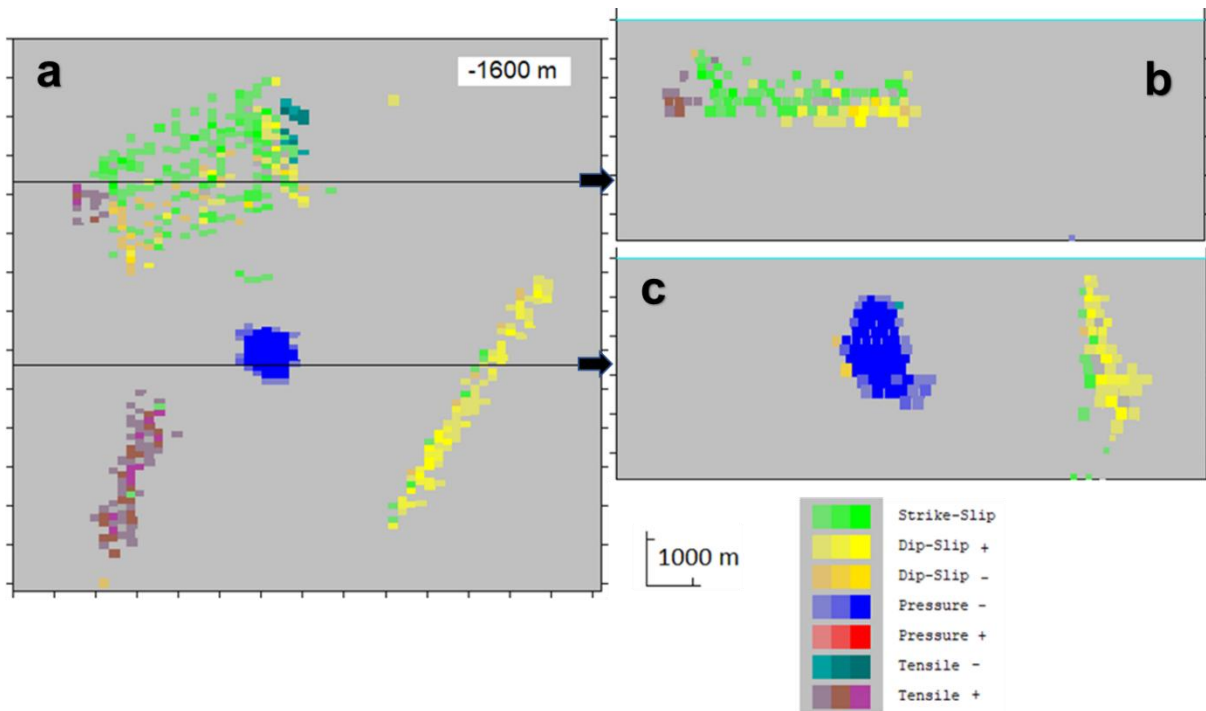
738

739

740

741

742



743

744 **Figure 5.** Inverse 3D source model as aggregation of elemental cells. (a) Horizontal sections

745 at 1500 m depth; (b) EW vertical profile across the strike structure (green cells); (c) EW

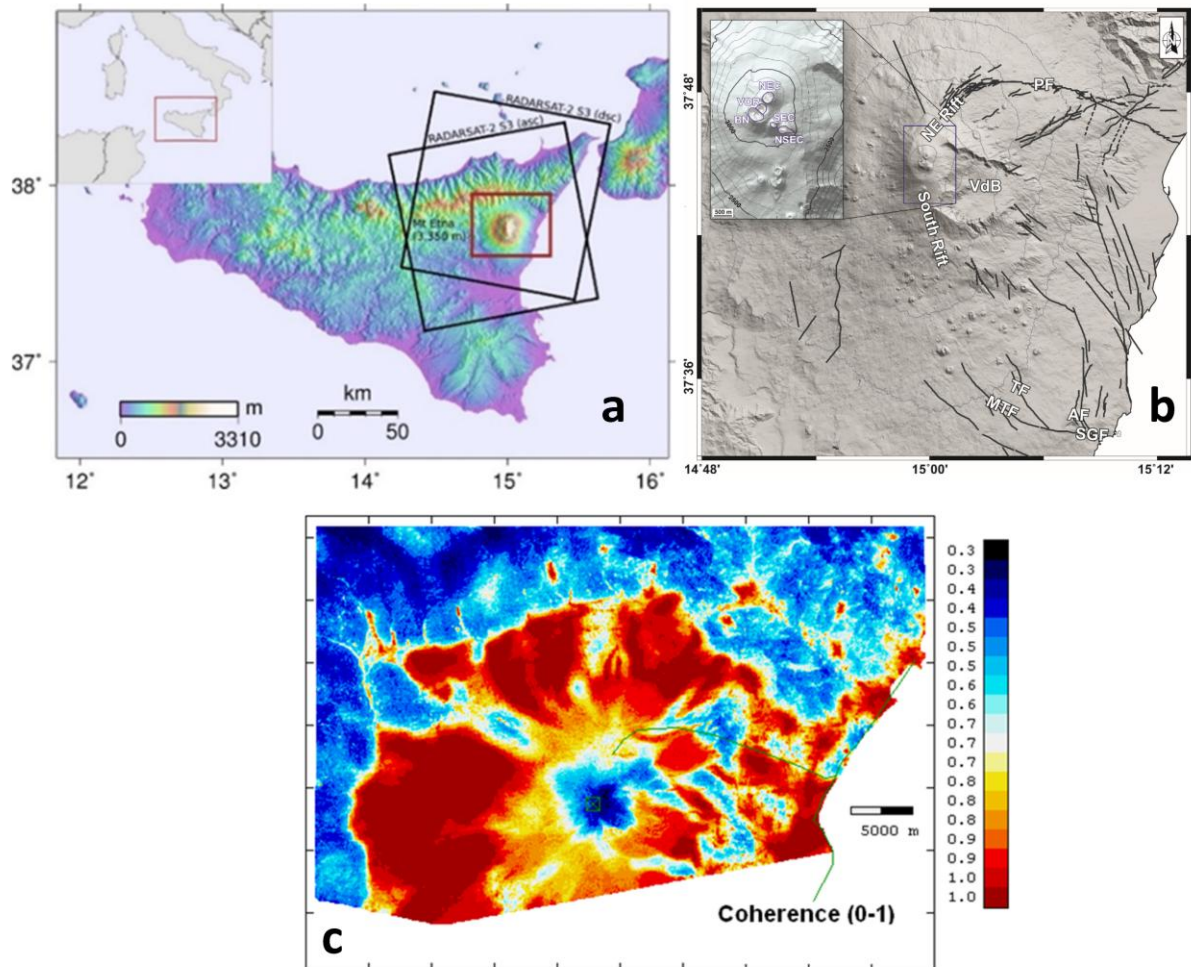
746 vertical profile across the low pressure structure (blue cells) and dip-slip structure (yellow

747 cells). Modelling magnitudes are 0.5 MPa and 1.5 cm.

748

749

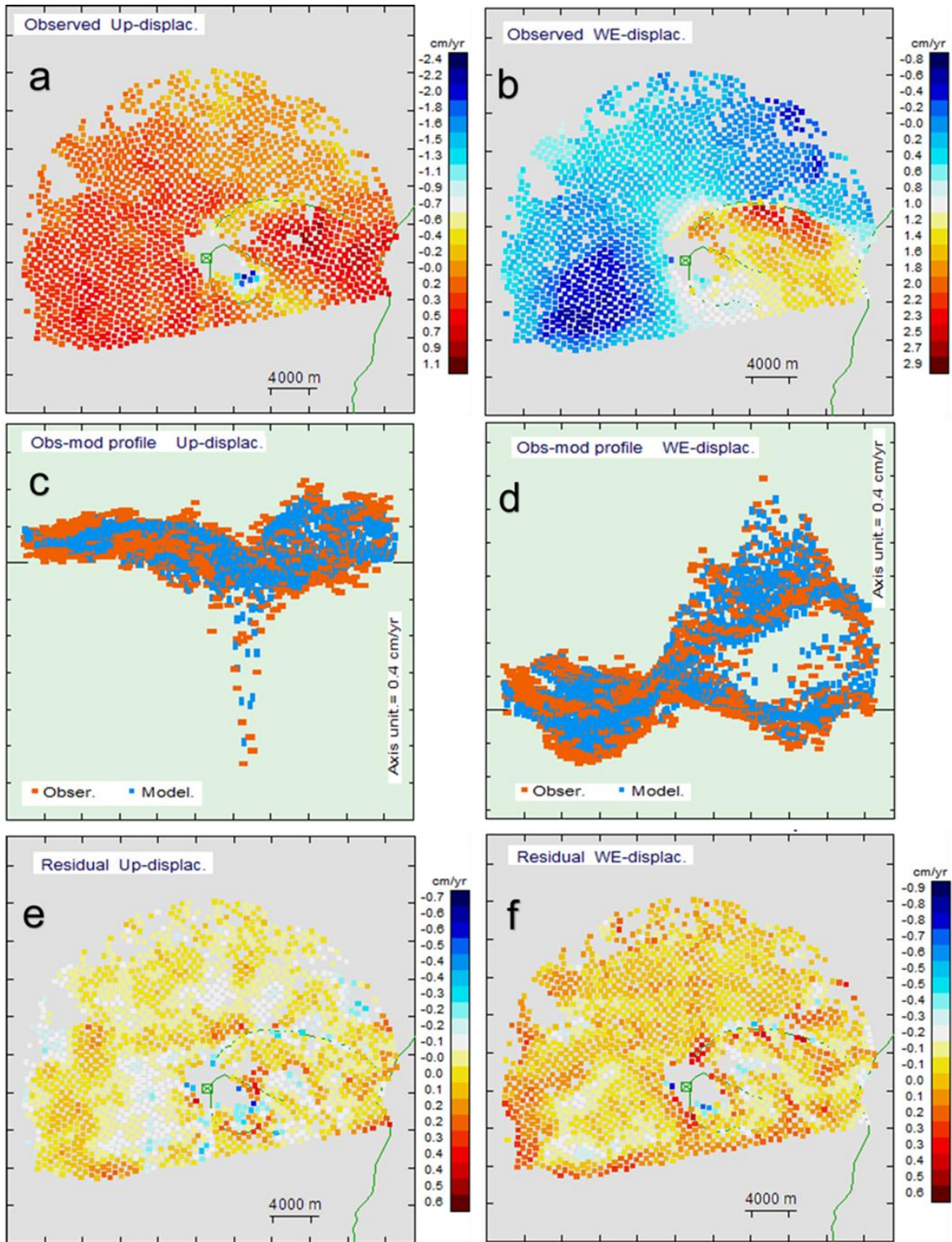
750



751

752 **Figure 6.** (a) Study area (outlined in an inner red square) and RADARSAT-2 frames
753 outlined in black. (b) Simplified tectonic map of Mt. Etna. Abbreviations are as follows: PF,
754 Pernicana fault; AF, Acitrezza fault; TF, Trecastagni fault; MTF, Mascalucia-Tremestieri
755 fault; VdB, Valle del Bove. Inset shows a zoom of the volcano summit (Bocca Nuova, BN;
756 Voragine, VOR; North-East Crater, NEC; South-East Crater, SEC; New South-East Crater,
757 NSEC). (c) InSAR pixels for the period January 2009 – June 2013 at Mt. Etna. Colours
758 correspond to coherence values.

759



760

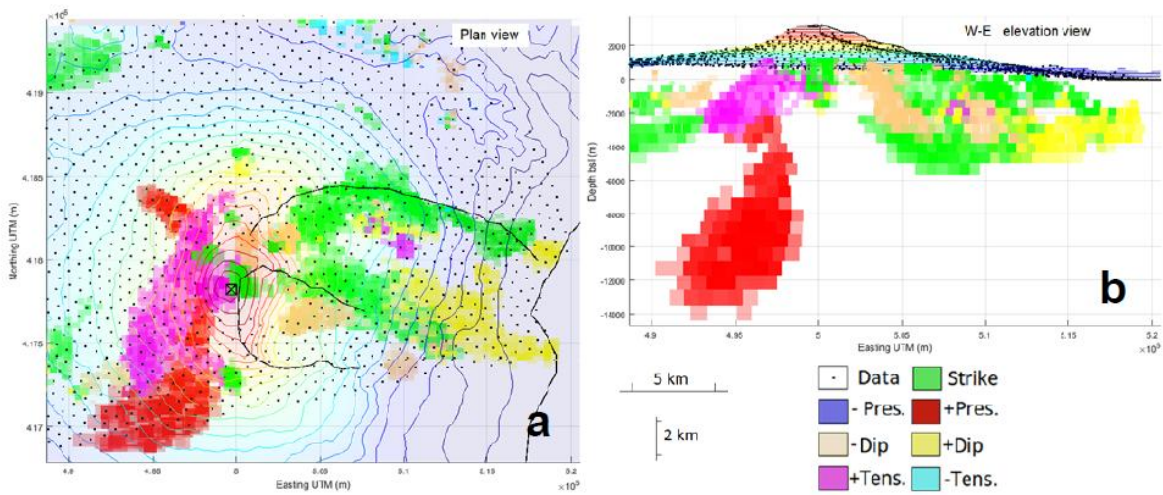
761 **Figure 7.** Observed displacement rate (cm/year): (a) Vertical and (b) EW component for the
 762 1613 pixels selected from the total dataset (Figure 6). Comparison between observed and
 763 modelled values: (c) Vertical and (d) EW component. Final residuals corresponding to local
 764 effects: (e) Vertical and (f) EW component.

765

766

767

768



769

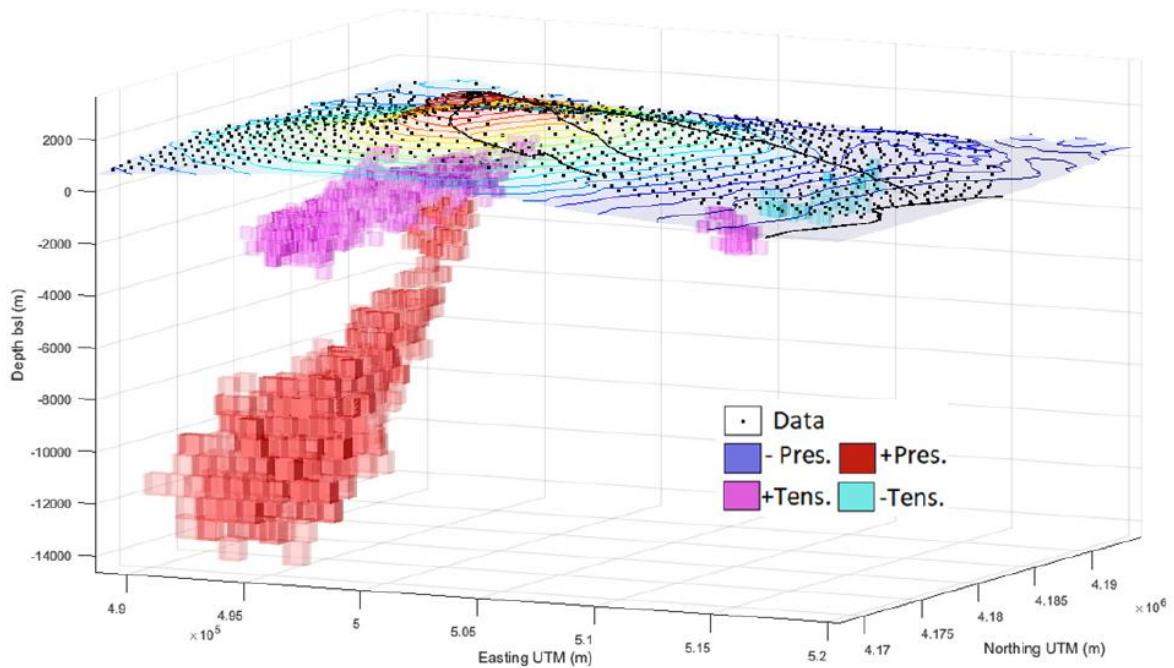
770 **Figure 8.** 3D inverse model described as aggregation of approximately 12,000 different
771 elemental cells (~ 440 m on a side), and obtained by application of the inverse approach: (a)
772 Planar and (b) EW vertical views. Colours indicate the source nature of the cell. Black lines
773 denotes the Permiana Fault, Valle del Bove limit and coast line (see Figure 6).

774

775

776

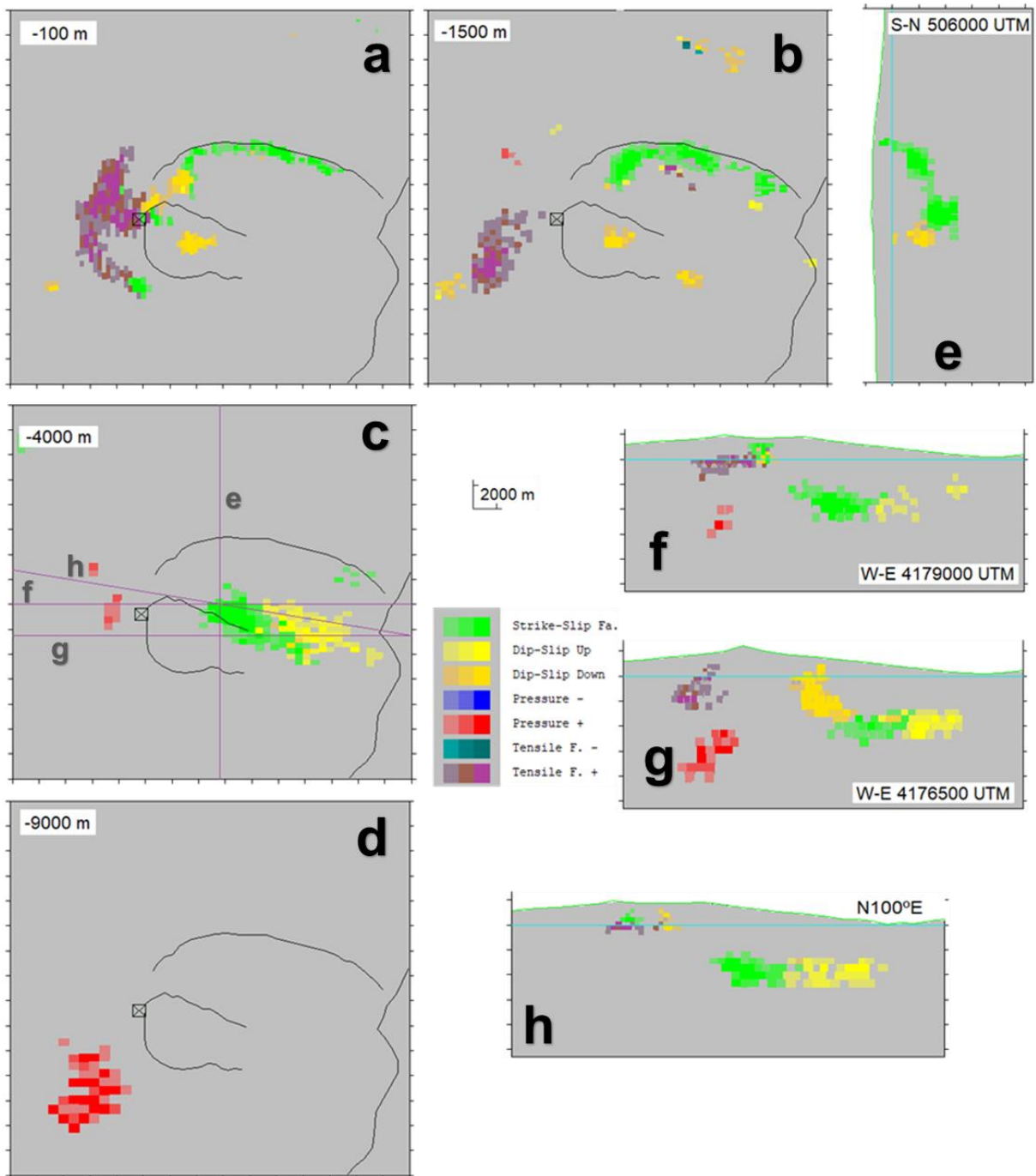
777



778

779 **Figure 9.** Perspective 3D view of those source elements in Figure 6 corresponding to the
780 plumbing system: increasing pressure cells (large deep reservoir with mean depth ~11 km bsl,
781 SW of Etna, and shallow small reservoir with mean depth 3 km bsl. NW of Etna and along the
782 elongation of the deep reservoir), and expanding tensile cells (at levels 1 km and 2 km bsl,
783 with elongated pattern SW-NW). Black lines correspond to Etna summit, Pernicana Fault and
784 Valle del Bove limit (see Figure 6).

785



786

787 **Figure 10.** Some horizontal and vertical sections of the tensile structure (purple), strike-slip
 788 structure (green), dip-slip structure (yellow) and high pressure (red) from the inverse model.
 789 (a),(b),(c) and (d): Horizontal sections at depths 500, 1000, 4000 and 9000 m bsl. (e) SN
 790 vertical section across the strike structure. (f) and (g): WE vertical sections. (h) Vertical
 791 section with azimuth 100°. Green lines correspond to Etna summit, Pernicana Fault and Valle
 792 del Bove. Location of vertical sections (e) to (h) are indicated by lines in panel (c).

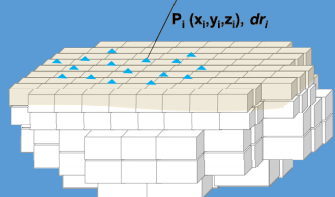
793

Methodology

Displacement data (dx, dy, dz):

- DInSAR
- GNSS
- Leveling
- ...

3D grid of (empty) cells to be filled by elementary sources.



Elastic parameters.
Dislocations and pressure anomalies.

Model Equations

$$dr^c = \sum_{\Phi_p} \begin{pmatrix} u_x \\ u_y \\ u_z \end{pmatrix} + \sum_{(\Phi_s, \Phi_D, \Phi_T)} \begin{pmatrix} u_x \\ u_y \\ u_z \end{pmatrix}$$

$$dr_j^c = \sum_{i \in \Phi_p} \Delta V_i \Delta \rho_i f_p(r_{ij}) + \sum_{i \in \Phi_s} \Delta S_i \Delta \sigma_i f_s(r_{ij}, \alpha_i, \delta_i) + \sum_{i \in \Phi_D} \Delta S_i \Delta \sigma_i f_D(r_{ij}, \alpha_i, \delta_i) + \sum_{i \in \Phi_T} \Delta S_i \Delta \sigma_i f_T(r_{ij}, \alpha_i, \delta_i)$$

$j=1, \dots, n$

.....

.....

Minimization condition

$$\varepsilon^T Q_D^{-1} \varepsilon = \min$$

Smoothing conditions

$$m^T Q_M^{-1} m = \min$$

Mixed minimization equation

$$\varepsilon^T Q_D^{-1} \varepsilon + \gamma m^T Q_M^{-1} m = \min$$

Growth process (scale factor)

Nearly automatic inversion process

3D Anomalous Sources

Extended 3D model for structures of anomalous pressure and dislocations defined as aggregation of cells filled with elementary sources.

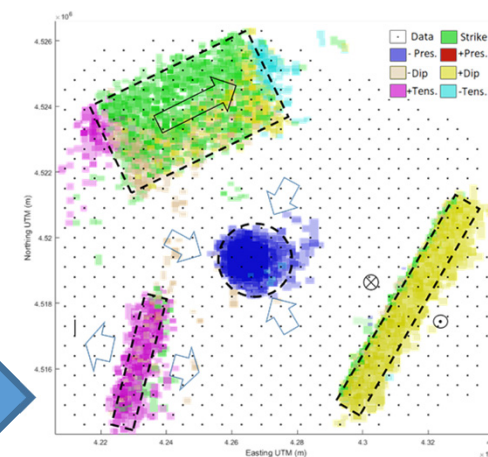


Figure 1
[Click here to download Figure: Figure1.pdf](#)

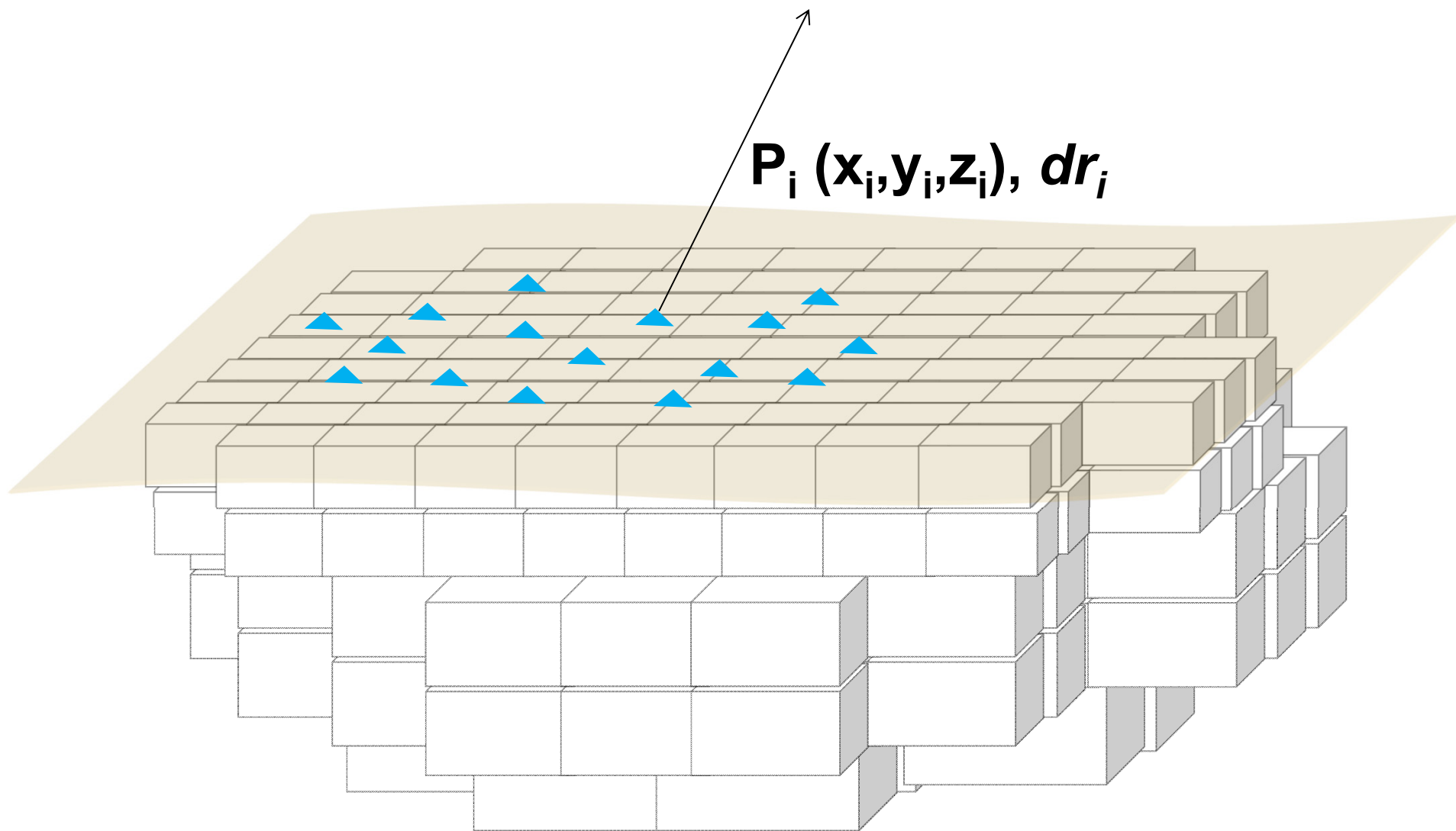


Figure 2
[Click here to download Figure: Figure2.pdf](#)

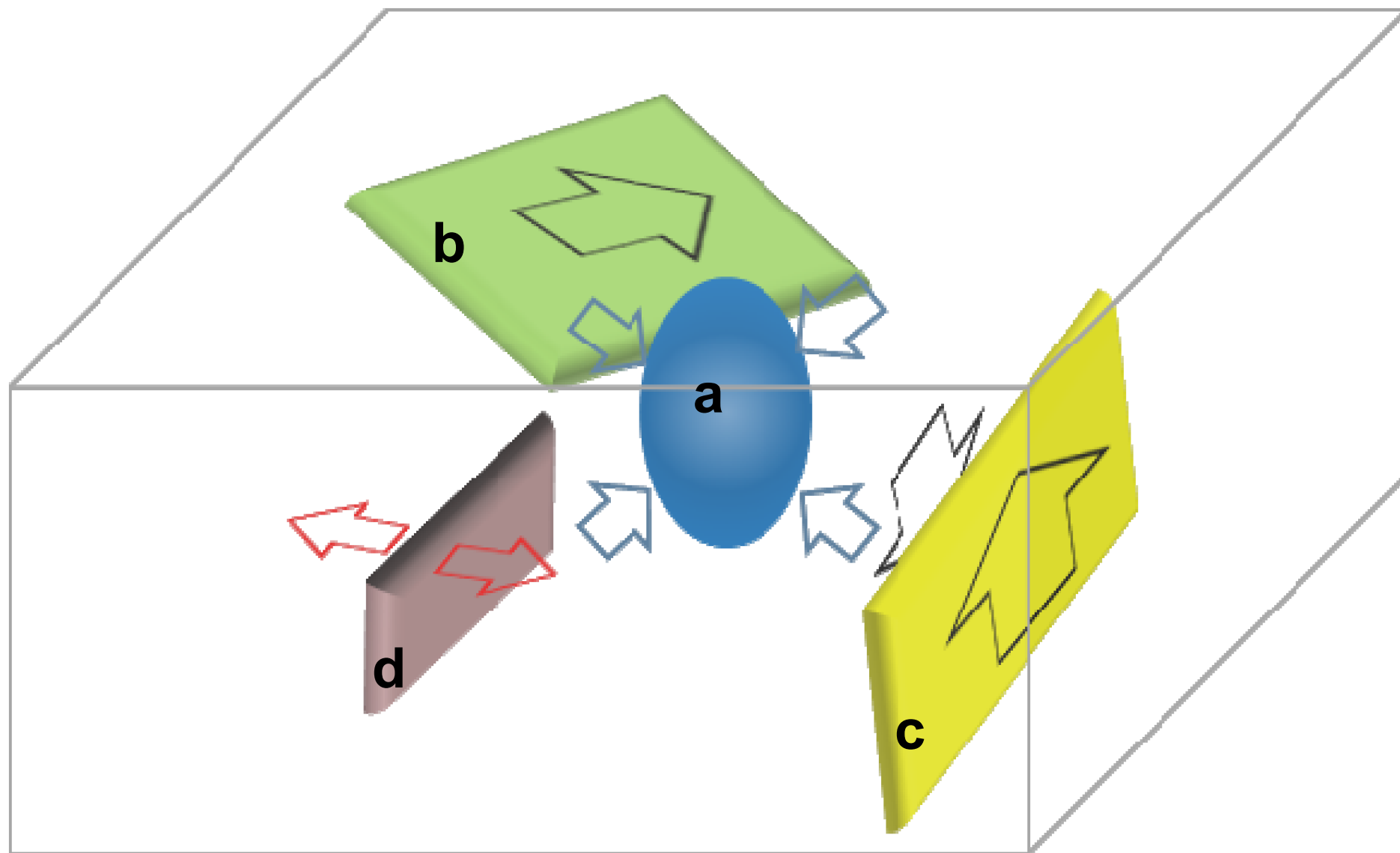


Figure 3
[Click here to download Figure: Figure3.pdf](#)

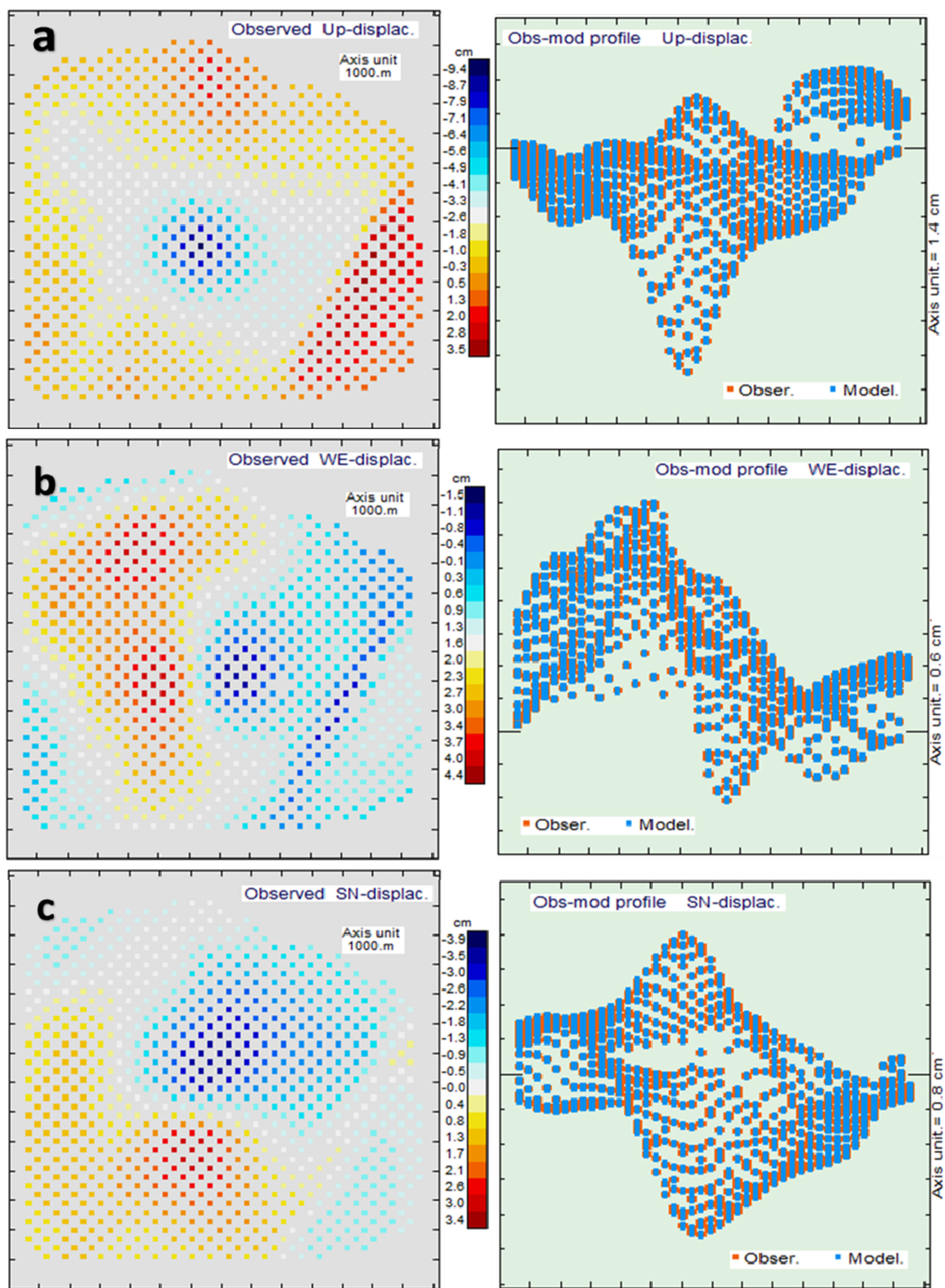


Figure 4

[Click here to download Figure: Figure4.pdf](#)

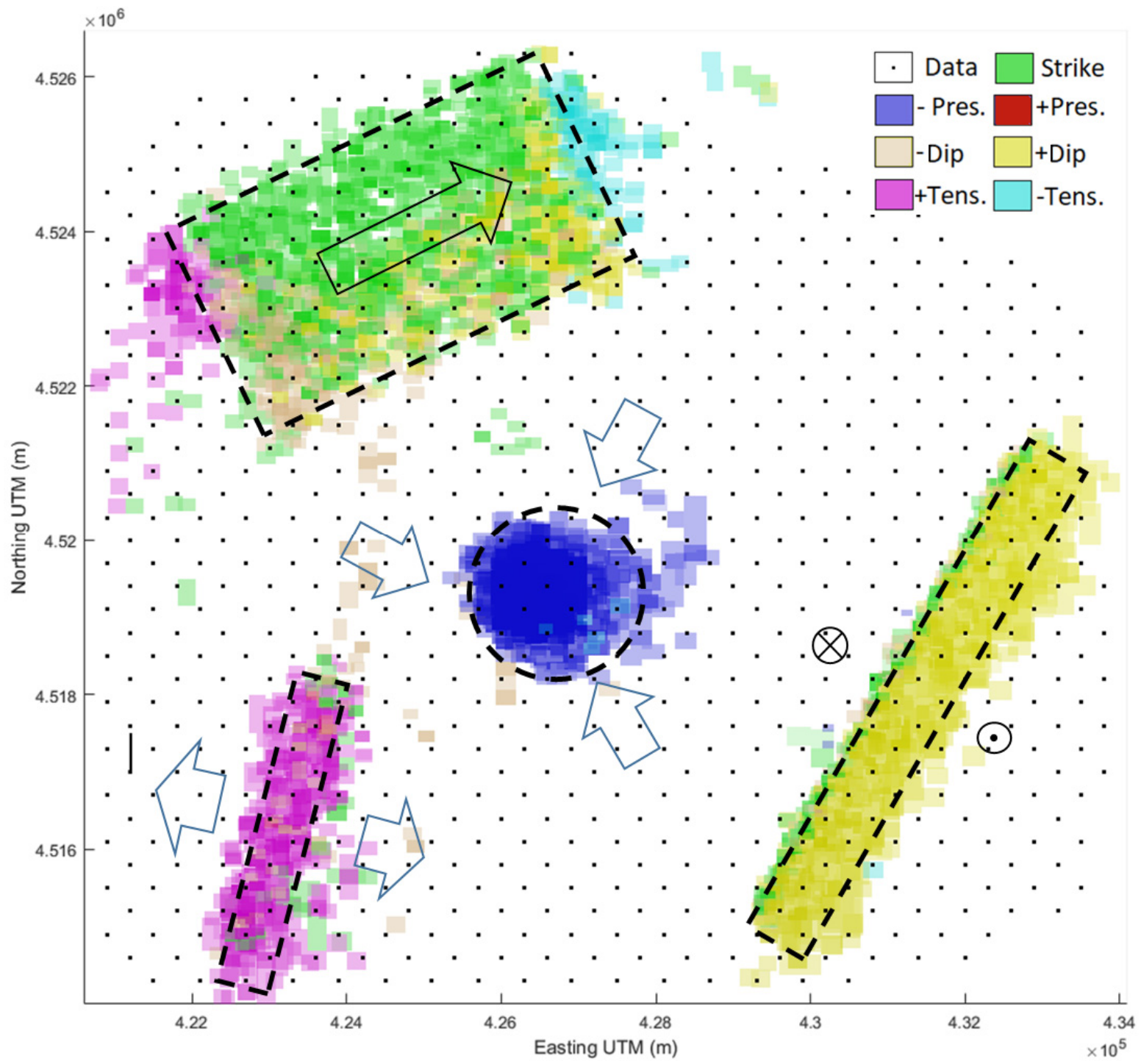


Figure 5
[Click here to download Figure: Figure5.pdf](#)

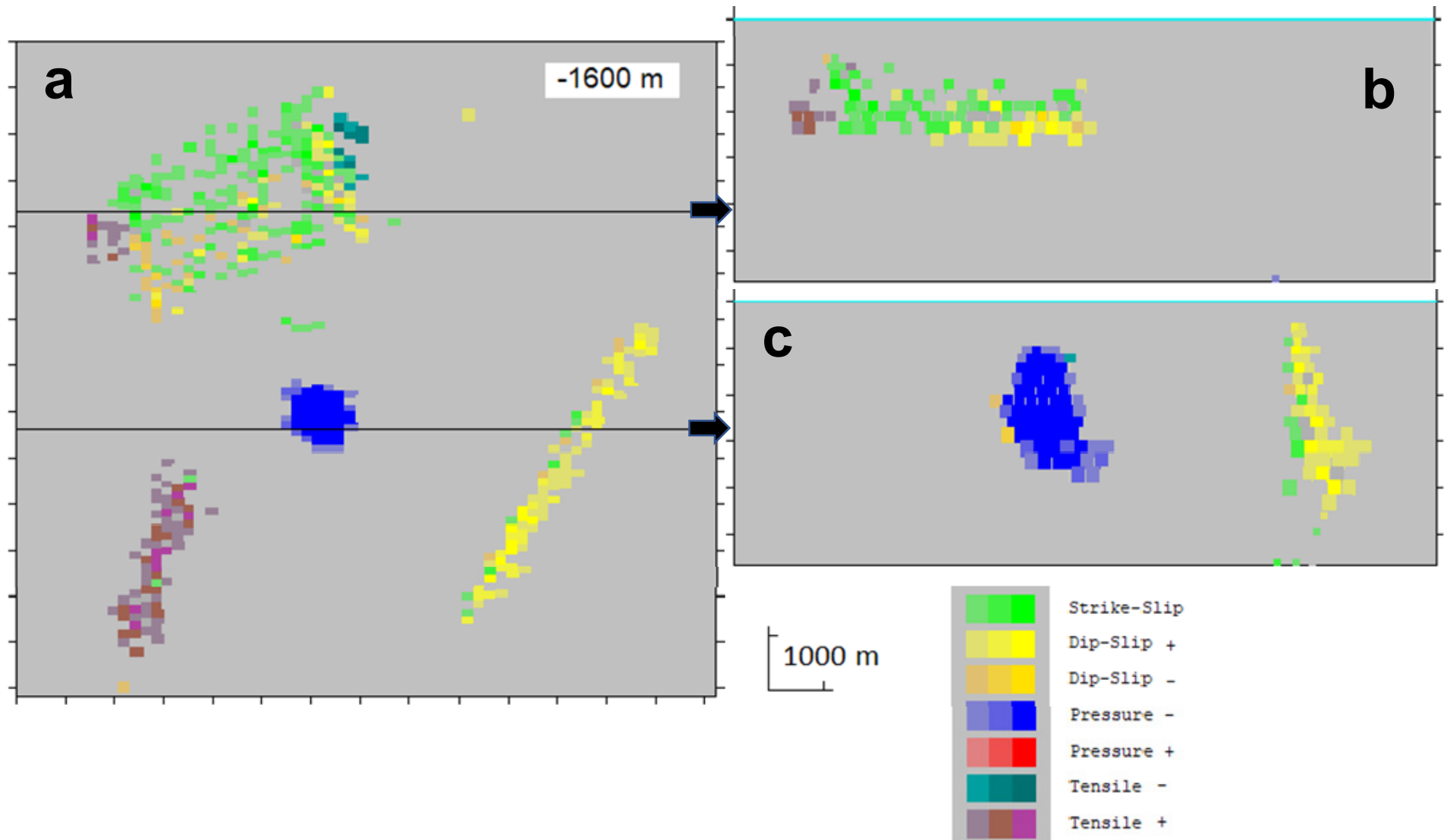


Figure 6
[Click here to download Figure: Figure6.pdf](#)

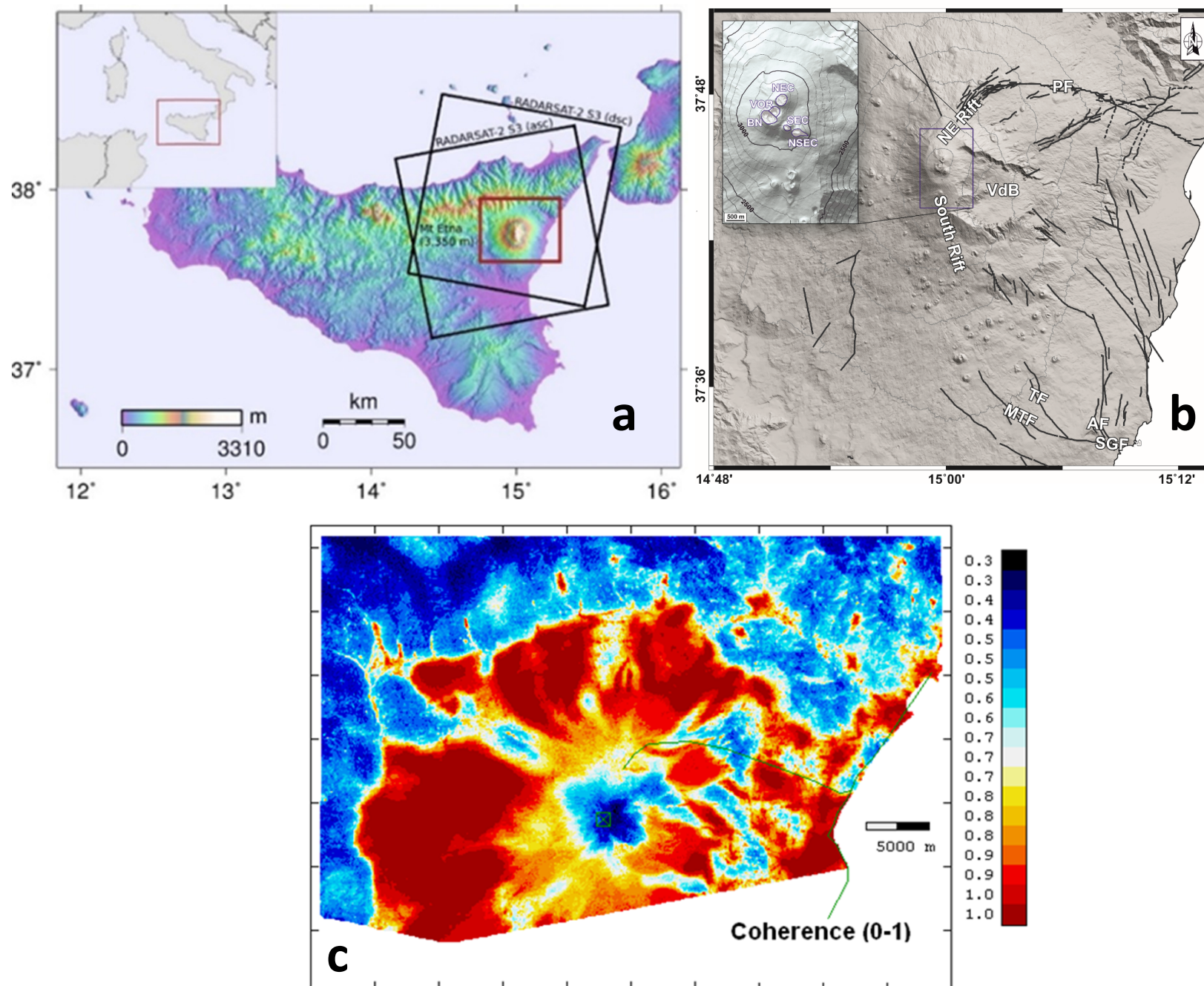


Figure 7
Click here to download Figure: Figure7.pdf

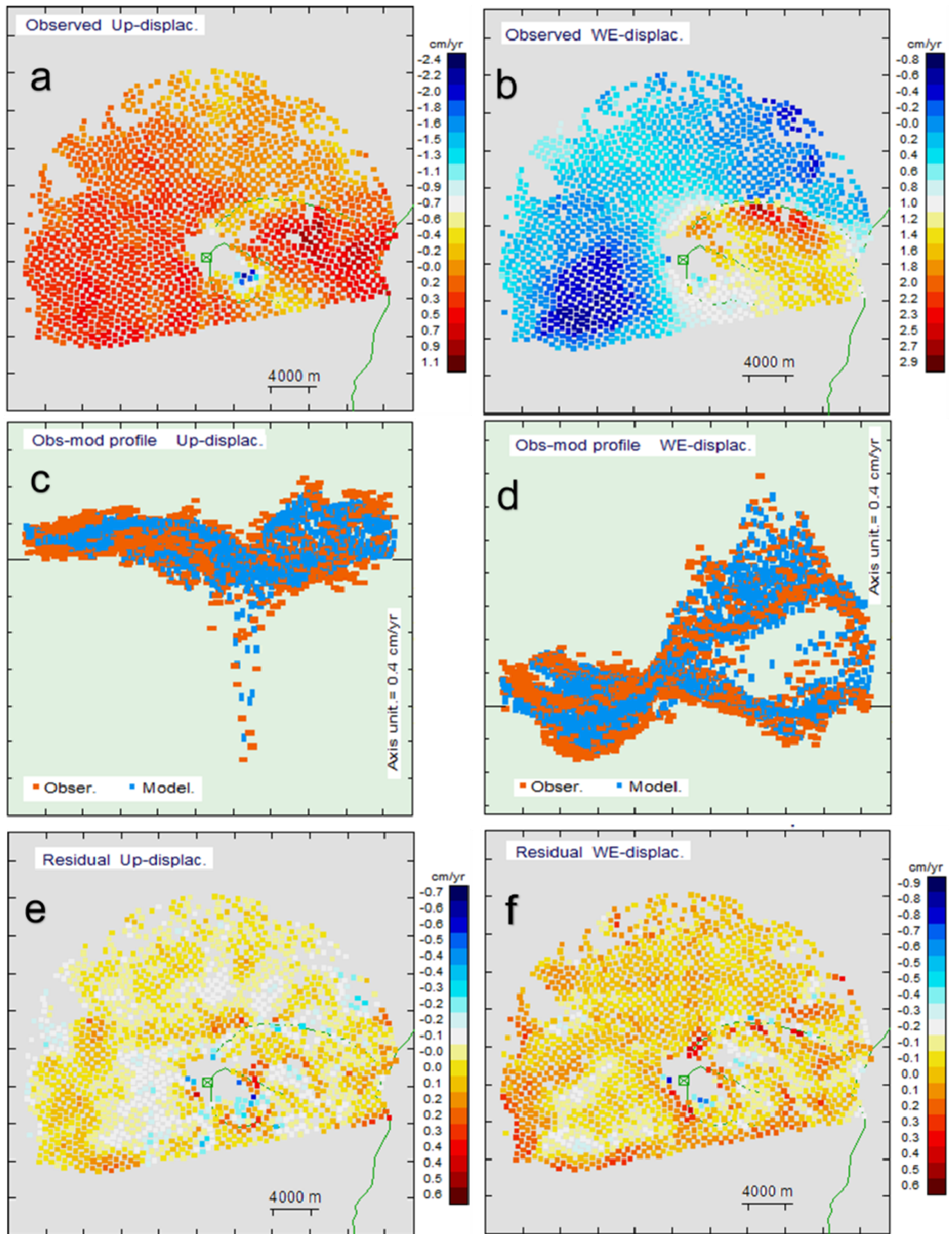


Figure 8

[Click here to download Figure: Figure8.pdf](#)

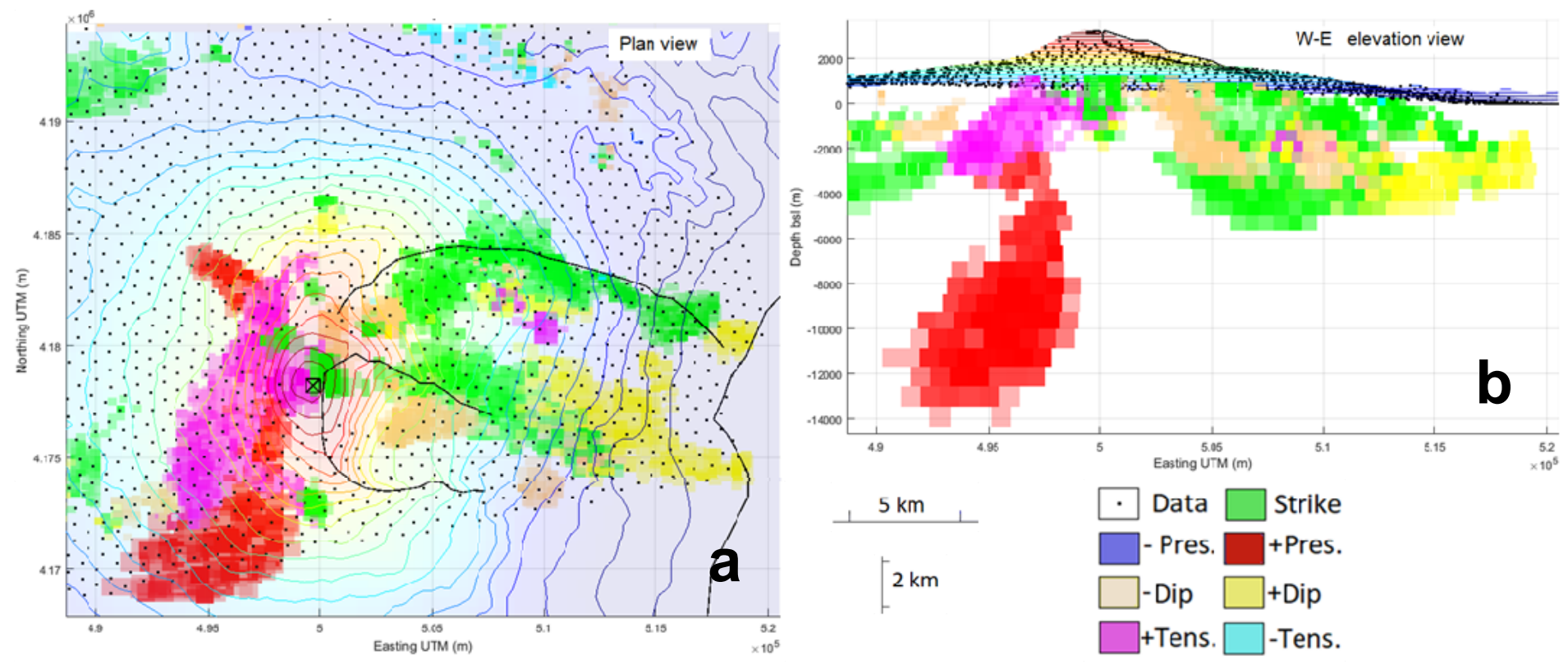


Figure 9

[Click here to download Figure: Figure9.pdf](#)

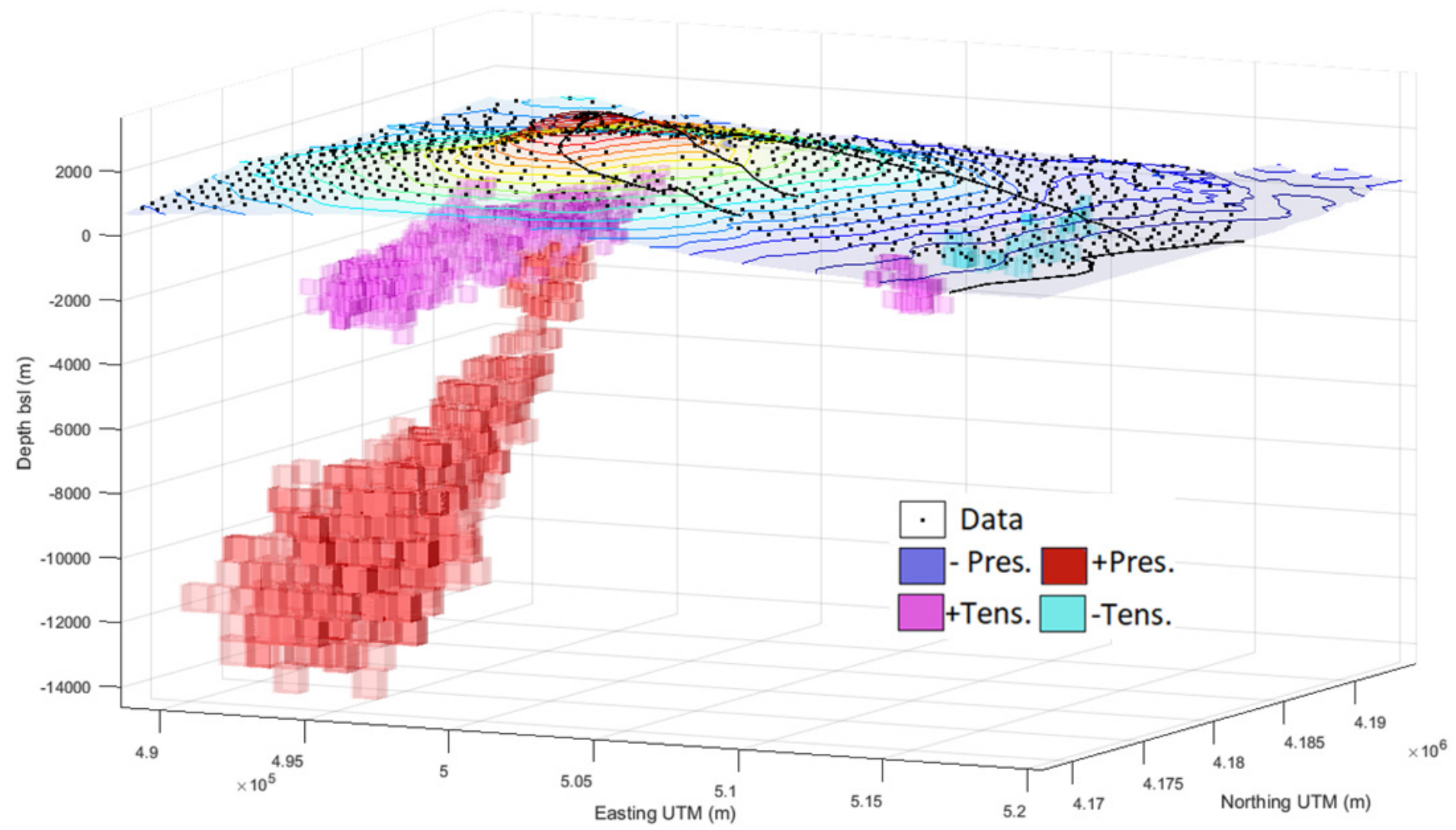
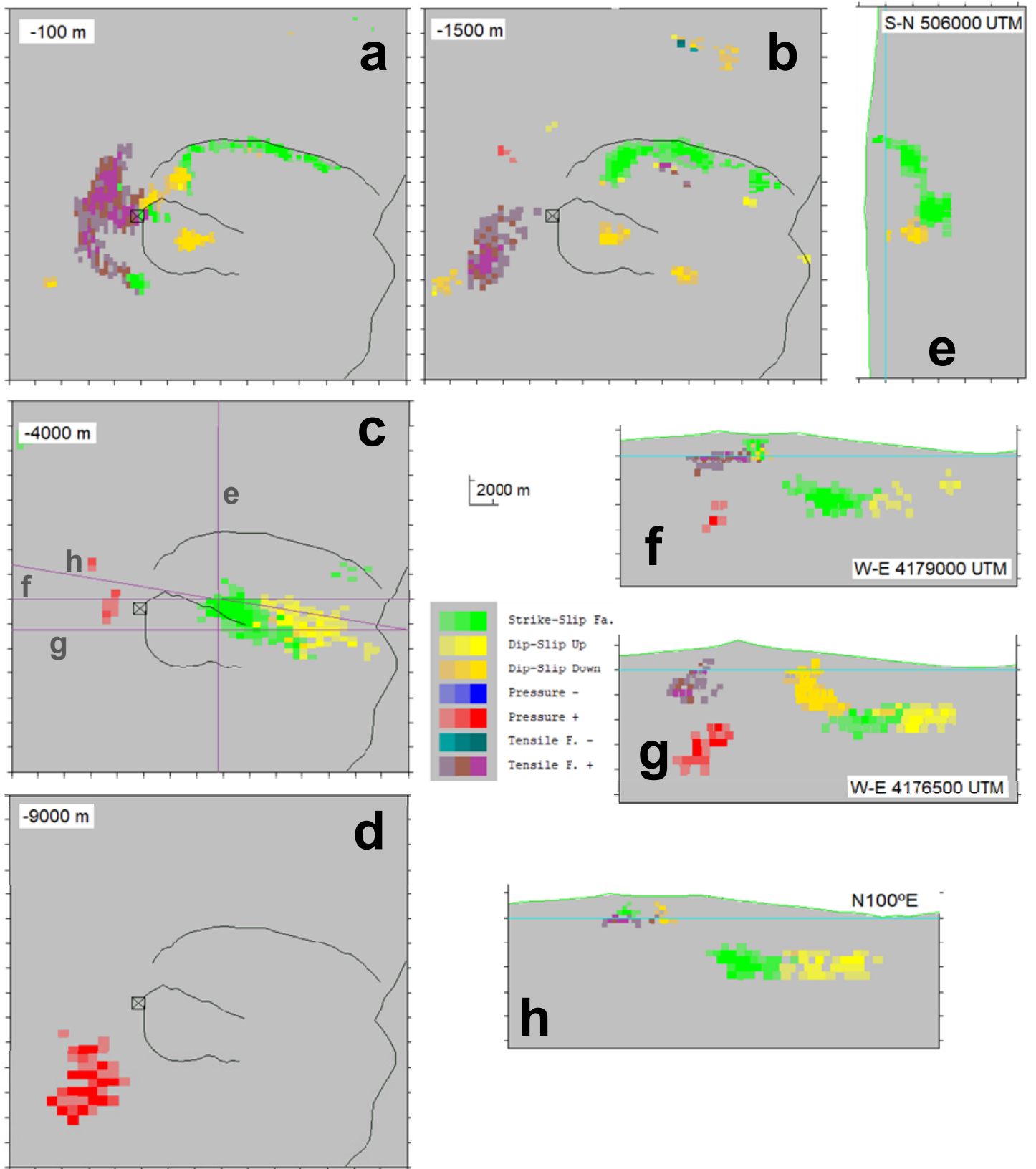


Figure 10
Click here to download Figure: Figure10.pdf



Supplementary material for online publication only

[Click here to download Supplementary material for online publication only: Camacho_et_al_2020_EPSL_SM_rev.pdf](#)

Declaration of interests

The authors declare that they have no known competing financial interests or personal relationships that could have appeared to influence the work reported in this paper.

The authors declare the following financial interests/personal relationships which may be considered as potential competing interests:

CRedit author statement

Antonio G. Camacho: Conceptualization, Methodology, Software, Validation, Formal Analysis, Investigation, Writing-Original Draft, Writing-Review & Editing, Funding acquisition. **José Fernández:** Conceptualization, Methodology, Software, Validation, Formal Analysis, Investigation, Writing-Original Draft, Writing-Review & Editing, Project administration, Funding acquisition. **Sergey V. Samsonov:** Formal analysis, Investigation, Data curation, Writing-Review & Editing. **Kristy F. Tiampo:** Formal Analysis, Investigation, Data curation, Writing-Review & Editing. **Mimmo Palano:** Formal Analysis, Investigation, Writing-Review & Editing.